Diurnal cycle of the semi–direct effect from a persistent absorbing aerosol layer over marine stratocumulus in large–eddy simulations

Atmos. Chem. Phys., 20, 1317–1340, 2020
https://doi.org/10.5194/acp-20-1317-2020

Atmospheric Chemistry and Physics
Open Access
EGU

Diurnal cycle of the semi-direct effect from a persistent absorbing aerosol layer over marine stratocumulus in large-eddy simulations

Ross J. Herbert[1,a], **Nicolas Bellouin**[1], **Ellie J. Highwood**[1], **and Adrian A. Hill**[2]

[1]Department of Meteorology, University of Reading, Reading, RG6 6BB, UK
[2]Met Office, Fitzroy Road, Exeter, EX1 3PB, UK
[a]now at: Department of Physics, University of Oxford, Oxford, OX1 3PU, UK

Correspondence: Ross J. Herbert (ross.herbert@physics.ox.ac.uk)

Received: 23 April 2019 – Discussion started: 4 June 2019
Revised: 12 November 2019 – Accepted: 8 January 2020 – Published: 5 February 2020

Abstract. The rapid adjustment, or semi-direct effect, of marine stratocumulus clouds to elevated layers of absorbing aerosols may enhance or dampen the radiative effect of aerosol–radiation interactions. Here we use large-eddy simulations to investigate the sensitivity of stratocumulus clouds to the properties of an absorbing aerosol layer located above the inversion layer, with a focus on the location, timing, and strength of the radiative heat perturbation. The sign of the daily mean semi-direct effect depends on the properties and duration of the aerosol layer, the properties of the boundary layer, and the model setup. Our results suggest that the daily mean semi-direct effect is more elusive than previously assessed. We find that the daily mean semi-direct effect is dominated by the distance between the cloud and absorbing aerosol layer. Within the first 24 h the semi-direct effect is positive but remains under 2 W m^{-2} unless the aerosol layer is directly above the cloud. For longer durations, the daily mean semi-direct effect is consistently negative but weakens by 30 %, 60 %, and 95 % when the distance between the cloud and aerosol layer is 100, 250, and 500 m, respectively. Both the cloud response and semi-direct effect increase for thinner and denser layers of absorbing aerosol. Considerable diurnal variations in the cloud response mean that an instantaneous semi-direct effect is unrepresentative of the daily mean and that observational studies may underestimate or overestimate semi-direct effects depending on the observed time of day. The cloud response is particularly sensitive to the mixing state of the boundary layer: well-mixed boundary layers generally result in a negative daily mean semi-direct effect, and poorly mixed boundary layers result in a positive daily mean semi-direct effect. The properties of the boundary layer and model setup, particularly the sea surface temperature, precipitation, and properties of the air entrained from the free troposphere, also impact the magnitude of the semi-direct effect and the timescale of adjustment. These results suggest that the semi-direct effect simulated by coarse-resolution models may be erroneous because the cloud response is sensitive to small-scale processes, especially the sources and sinks of buoyancy.

1 Introduction

Semi-permanent decks of marine stratocumulus clouds represent an important negative radiative effect within the Earth's energy budget (Hartmann et al., 1992; Hartmann and Short, 1980; Wood, 2012). In addition, the sharp inversion layer and small-scale turbulent processes that characterize the formation and maintenance of these clouds represent considerable uncertainty in climate models, so stratocumulus clouds remain a key uncertainty in future climate projections (Bony and Dufresne, 2005; Klein et al., 2017; Wood, 2012). Marine stratocumulus clouds are sensitive to sea surface temperature (SST) and large-scale atmospheric properties above the inversion, like the subsidence rate and thermodynamic properties of the overlying air mass, and below the inversion, like cloud condensation nuclei sinks and sources, that impact turbulent processes and dynamics throughout the boundary layer (e.g. Bretherton et al., 2013; Feingold et al., 2010; Sandu et al., 2010). Therefore, small changes to these properties could result in large changes to the fluxes of radiation in the atmosphere.

Perturbations to the aerosol distribution result in a radiative forcing through both aerosol–radiation and aerosol–cloud interactions; this distinction separates the radiative forcing caused by aerosol scattering and absorption of longwave and shortwave radiation from that caused by the availability of cloud condensation nuclei. Aerosol–cloud interactions lead to changes in cloud albedo and subsequent rapid adjustments to the cloud properties that include changes to precipitation and cloud evolution (Sherwood et al., 2015). Aerosol–radiation interactions result in instantaneous changes to the extinction profile (also referred to as the direct radiative effect) and therefore the heating profile, which lead to rapid adjustments in the physical and radiative properties of the cloud (referred to in this paper as the semi-direct effect, SDE, for convenience). Quantifying rapid adjustments is important as they may act to dampen or strengthen the instantaneous forcing. Aerosol–radiation interactions represent an important uncertainty in the anthropogenic radiative forcing of the climate over the industrial era, especially from absorbing aerosol species such as black carbon, which may result in pronounced semi-direct effects (Boucher et al., 2013). In a recent climate model intercomparison study Stjern et al. (2017) found that a tenfold increase in black carbon emissions resulted in a strong positive direct effect that was partially offset by a negative SDE. Although all models agree on the sign (negative) they disagree on the size of that offset, from 12 % to 63 % for the models studied by Stjern et al. (2017). High-resolution models that can sufficiently represent the dominant processes within the boundary layer and cloud are a powerful benchmark to test the realism of the response simulated by climate-scale models.

During the African dry season, which lasts from August to October, plumes of strongly absorbing biomass burning aerosol from central Africa are transported westward over the semi-permanent marine stratocumulus deck of the southeast Atlantic Ocean, where they eventually subside and mix into the boundary layer (Das et al., 2017). Observational and modelling studies suggest that elevated absorbing layers result in thicker clouds and a negative SDE (Adebiyi and Zuidema, 2018; Johnson et al., 2004; Wilcox, 2010), which may impact the stratocumulus-to-cumulus transition process (Yamaguchi et al., 2015; Zhou et al., 2017). Once mixed into the cloud layer the absorbing aerosol exerts aerosol–radiation interactions that enhance cloud evaporation (Hill and Dobbie, 2008; Johnson et al., 2004) and aerosol–cloud interactions that impact microphysical and dynamical processes (e.g. Feingold et al., 2010; Gordon et al., 2018; Hill et al., 2009). Observational studies have used satellite retrievals from the NASA A-Train to investigate the interaction between clouds and absorbing aerosol over the southeast Atlantic. Wilcox (2010) used co-located CALIPSO, OMI, and AMSR-E retrievals and found that for all overcast scenes liquid water path (LWP) increased for high aerosol loading. This response was attributed to absorbing aerosol layers above the cloud top, enhancing the heating rate and decreasing entrainment across the inversion. However, satellites do not provide direct observations of entrainment and an alternative explanation could be that the aerosol layers travel in relatively moist layers (Adebiyi et al., 2015), increasing moisture transport across the inversion layer, even if entrainment remained unchanged. In a study with a similar methodology, Costantino and Bréon (2013) separated the CALIPSO-derived aerosol layer heights into cases when the smoke was close to (< 100 m) and well separated (< 750 m) from the cloud top. The authors found that when the aerosol layers are well separated from the cloud top the LWP and cloud optical thickness showed no statistically significant dependence on aerosol loading. These results are supported by Adebiyi and Zuidema (2018), who used satellite observations and reanalysis products to show evidence that the sensitivity of low cloud cover to elevated aerosol layers increased for small cloud–aerosol gaps. These observations suggest that the distance between the elevated aerosol layer and cloud layer plays an important role in the strength of the SDE. Additionally, a recent satellite study of cloud–aerosol gaps by Rajapakshe et al. (2017) suggests that the elevated aerosol layers may be closer to the cloud than previously thought, which demonstrates that elevated layers may have an even more important impact on the clouds.

The observations hint at the potential importance of the extent of cloud–aerosol gaps for the SDE. However, this complexity is not reflected in the frameworks presented in current reviews (Bond et al., 2013; Koch and Del Genio, 2010), and there is a lack of high-resolution modelling studies investigating the SDE from elevated layers of absorbing aerosol. Johnson et al. (2004) used large-eddy simulation (LES) to investigate the semi-direct effect of absorbing aerosols on non-precipitating marine stratocumulus. In an experiment in which a ~ 1 km thick layer of absorbing aerosol, with an aerosol optical depth (AOD) of 0.2 at 550 nm, was present above the marine boundary layer throughout a 48 h simulation, the absorbing aerosol enhanced the temperature inversion at the top of the boundary layer, weakening the entrainment rate across the inversion and producing a shallower, moister boundary layer and a higher LWP. The 48 h mean SDE was estimated to be $-9.5\,\mathrm{W\,m^{-2}}$, almost entirely cancelling a direct effect of $+10.2\,\mathrm{W\,m^{-2}}$. Yamaguchi et al. (2015) and Zhou et al. (2017) used LES models to investigate the transition of marine stratocumulus to cumulus in the presence of a smoke layer. As the marine boundary layer deepened, the cloud–aerosol gap decreased until the smoke layer made contact with the cloud layer. Both studies found little LWP response when the smoke layer was separated by a no-aerosol gap. Yamaguchi et al. (2015) found that the elevated smoke layer reduced boundary layer turbulence and cloud cover through a decrease in longwave cloud-top cooling. By isolating the aerosol heating above and below the boundary layer top, Zhou et al. (2017) found that when the layer was directly above the inversion layer the elevated aerosol layer strengthened the inversion, inhibiting en-

trainment, and increased LWP and cloud cover, resulting in a negative SDE. Global models have also been used to investigate the radiative impact of biomass burning aerosol in stratocumulus regions (e.g. Lu et al., 2018; Penner et al., 2003; Sakaeda et al., 2011); however, Das et al. (2017) show that these coarser-resolution models may be unable to reproduce the observed vertical distribution of absorbing aerosol layers over the southeast Atlantic, resulting in an underrepresentation of elevated aerosol layers and increased uncertainty in their radiative impact.

In summary, observation and modelling studies suggest that the diurnal cycle and evolution of marine stratocumulus are strongly impacted by the presence of absorbing aerosol layers at and above the top of the boundary layer. The SDE may act to counteract or enhance the direct effect, resulting in either a small or large net radiative effect from aerosol–radiation interactions. Yet the sensitivity of the SDE to the properties of the elevated aerosol layer has not been fully investigated. In this study the UK Met Office Large Eddy Model (LEM) is used to investigate and quantify the impact that the properties of a persistent elevated absorbing aerosol layer have on the cloud and radiative response of marine stratocumulus, with a focus on the role that the location, timing, and strength of the heat perturbation has in the underlying cloud and boundary layer. Section 2 presents the LEM and its configuration and introduces a set of experiments designed to assess the SDE and its sensitivity to the aerosol layer properties. Section 3 focuses on a single experiment to understand the processes that drive the cloud response and SDE, then assesses the sensitivity of this response to the aerosol layer properties. Section 3 also investigates the robustness of that assessment to the processes that affect the maintenance of the cloud, namely precipitation, sea surface temperature, and boundary layer depth. Section 4 summarizes the results by comparing to other modelling studies and observations and discusses the limitations of this study in addition to identifying remaining questions.

2 Model description and setup

2.1 Description of model

The LEM (Gray et al., 2001) is a non-hydrostatic high-resolution numerical model that explicitly resolves the large-scale turbulent motions responsible for the energy transport and flow. The LEM has a long track record of being used to study cloud–precipitation–aerosol interactions in several cloud regimes (e.g. Efstathiou et al., 2016; Efstathiou and Beare, 2015; Hill et al., 2009, 2014) and has been included in several LES intercomparison studies (e.g. Ackerman et al., 2009; van der Dussen et al., 2013; Ovchinnikov et al., 2014; de Roode et al., 2016). Sub-grid-scale turbulence responsible for the dissipation of kinetic energy is parameterized. Prognostic variables are the three-dimensional velocity fields (u, v, w), liquid water potential temperature (θ_l), and mass mixing ratios of water vapour (q_v), liquid water (q_l), and rain (q_r). Liquid water mass is prognosed at every grid point using a condensation–evaporation scheme in which excess supersaturation is converted to liquid water and vice versa for subsaturated air. Warm rain processes are represented by a single-moment microphysics scheme that includes autoconversion and cloud droplet collection following Lee (1989), sedimentation of rain, and evaporation of rain into dry air. The influence of aerosol on cloud droplet number concentration is not included in this study, and the cloud droplet number is fixed to $240\,\mathrm{cm}^{-3}$ for microphysical processes. Surface fluxes of moisture and heat are calculated using Monin–Obukhov similarity theory (Monin and Obukhov, 1954), which predicts the surface frictional stresses and heat fluxes using the local gradients between the surface and the overlying model level. For these experiments a prescribed constant sea surface temperature is used. A damping layer that relaxes all prognostic variables to their horizontal mean is present above an altitude of 775 m (~ 150 m above the cloud layer; see Sect. 2.2) with a height scale of 650 m and a timescale of 30 s. This prevents the reflection of gravity waves at the rigid top boundary and prevents the production of trapped buoyancy waves above the inversion layer (Ackerman et al., 2009). The subsidence rate w_s is represented by a height-dependent function $w_s(z) = -Dz$ for which large-scale divergence (D) is prescribed. The model is run with a variable time step with a maximum of 0.5 s. The LEM radiation scheme, described by Edwards and Slingo (1996), is a two-stream solver with six shortwave spectral bands and eight longwave bands that calculates the vertical distribution of radiative fluxes and heating rates. The scheme includes six aerosol species with wavelength- and humidity-dependent mass absorption coefficients, mass scattering coefficients, and asymmetry factors. A single value for the mean cloud droplet effective radius of 10 µm is prescribed in the radiation scheme.

2.2 Model setup

All simulations are three-dimensional with periodic lateral boundary conditions. The model domain is 5200 m in the horizontal, with a horizontal grid resolution of 40 m, and 2600 m in the vertical with a variable vertical grid resolution: ~ 6 m resolution at the cloud top and inversion but less than 10 m throughout the boundary layer (BL). The LEM is configured here to produce a stratocumulus with a consistent diurnal cycle over an 8 d timescale. The initial profiles of θ_l and q_t were taken from Johnson et al. (2004) and based on subtropical marine stratocumulus observations from the First International Satellite Cloud Climatology Project Regional Experiment (FIRE) (Hignett, 1991) in the subtropical Pacific Ocean. A series of 10 d simulations without absorbing aerosol were run with varying subsidence rates to obtain steady-state profiles of θ_l and q_t that would produce a consis-

Table 1. Initial profiles used in the control simulations.

Altitude (m)	Liquid water potential temperature (K)	Total water mixing ratio ($g\,kg^{-1}$)
0	287.5	9.0
600	287.5	9.0
601	297.0	5.5
750	300.0	5.5
1000	301.7	5.5
1500	303.2	5.5
2600	304.0	5.5

tent stratocumulus layer with a maximum cloud-top height of 600 m. The resulting initialization profiles are shown in Table 1; the BL is $0.6\,g\,kg^{-1}$ drier than in Johnson et al. (2004) and Hill et al. (2008) due to the inclusion of precipitation in our study and a cooler SST, which was necessary in order to attain a similar cloud LWP to these studies. The large-scale divergence D is set to $5.5 \times 10^{-6}\,s^{-1}$, giving a subsidence rate of $w_s = -3.3\,mm\,s^{-1}$ at the cloud top. D and w_s are within the observed range for marine stratocumulus regions (Zhang et al., 2009) and of similar magnitude to other stratocumulus LES studies (e.g. Johnson et al., 2004; De Roode et al., 2014). The initial profiles describe a well-mixed moist BL capped by a sharp (10 K) inversion at 600 m with a warm and dry free troposphere (FT) above the inversion. To account for a source of large-scale heat divergence a cooling rate of $0.1\,K\,d^{-1}$ is applied. This value is lower than the $1.0\,K\,d^{-1}$ used by Johnson et al. (2004) and Hill et al. (2008) because the greater cooling rates result in an unstable cloud-top height in our simulations, which is undesirable as we require a consistent cloud layer to isolate the cloud response due to the absorbing aerosol. A prescribed surface pressure of 1012.5 hPa is used, and zonal and meridional geostrophic winds are 6.0 and $-1.0\,m\,s^{-1}$, respectively. The radiation scheme is set up for consistency with the FIRE campaign with a time-varying solar zenith angle for mid-July at the coordinates 33° N, 123° W. Radiation calculations are performed for all grid points within the domain every 30 s. Surface roughness is fixed at 2×10^{-4} m and SST at 287.2 K.

2.3 Setup of elevated–aerosol experiments

To simulate the effect of an elevated absorbing aerosol layer above the cloud top, a layer of dry aerosol is prescribed, consisting of soot-like and water-soluble-like aerosol, representing predominantly absorbing and scattering species, respectively. The interaction of longwave and shortwave radiation with the aerosol layer results in localized heating rates that are coupled to the LEM. The prescribed aerosol layer properties include the height of the layer base above the inversion layer (referred to as the cloud–aerosol gap), geometric thickness, mean single-scattering albedo (SSA), and AOD. These properties are set at the beginning of the experiment and applied during each call to the radiation scheme. Using the prescribed geometric thickness of the aerosol layer, a balance between the mass mixing ratio of soot and water-soluble aerosol is used to achieve the desired SSA and AOD throughout the simulation (see Appendix A for more details on the method employed). In these experiments SSA is 0.9, which is towards the higher end of the range of SSA for biomass burning aerosol (Peers et al., 2016) and thus represents a relatively conservative value for the absorption of the aerosol layer.

Realistic cloud–aerosol gaps are needed for the elevated aerosol experiments. They are taken from observations from the CALIPSO Cloud–Aerosol Lidar with Orthogonal Polarization (CALIOP) instrument (5 km resolution, 532 nm Aerosol Layer Product and Cloud Layer Product, v4.10, level 2 data) and the NASA Cloud–Aerosol Transport System (CATS) lidar (5 km resolution, V3-00, mode 7.2, level 2 Daytime Operational Layer Data Product, 1064 nm wavelength) over the southeast Atlantic Ocean (15° S to 2.5° N, 10° W to 10° E). The distance Δz between the retrieved cloud-top and the aerosol base heights is determined from scenes in which vertical profiles only include a single layer of low cloud (cloud top below 2.5 km) and a single layer of aerosol. Figure 1 shows the normalized frequency of occurrence of Δz in 2.5° grids for all scenes within July, August, and September between 2007 and 2016 for CALIOP data and between 2015 and 2017 for CATS data. Both datasets display considerable variation in Δz at all locations, yet the CATS dataset has a higher percentage of scenes in close proximity (within 360 m) to the cloud top compared to CALIOP. This agrees well with the study of Rajapakshe et al. (2017), who found that the 532 nm wavelength used in the CALIOP retrieval often overestimates the distance between the cloud top and aerosol base, whereas the longer 1064 nm wavelength used by CATS provides a more reliable estimate. The CALIOP and CATS analysis (Fig. 1) suggests that elevated aerosol layers predominantly exist within 1500 m of the cloud top, with a common occurrence of layers in close proximity (less than 360 m) to the cloud. In line with this we focus on layers of absorbing aerosol that range from directly above the cloud layer ($\Delta z = 0$ m) to elevated layers at $\Delta z = 500$ m, and we additionally examine the role of the aerosol layer depth, which, for a given AOD, will impact the vertical distribution and strength of the localized heat perturbation.

A schematic of the experiments designed to investigate the sensitivity of the SDE and cloud diurnal cycle to key layer properties, namely the AOD, geometric thickness, and the cloud–aerosol gap, is shown in Fig. 2. The first set investigates the sensitivity of the SDE to the strength of the aerosol layer absorption. Following AOD observations by Chand et al. (2009), the AOD of the layer is varied from 0.1 to 0.5 while keeping the geometric thickness constant at 200 m and the cloud–aerosol gap at 50 m. The second set of experiments investigates the sensitivity of the cloud response to the geometric thickness of the aerosol layer at constant AOD. This

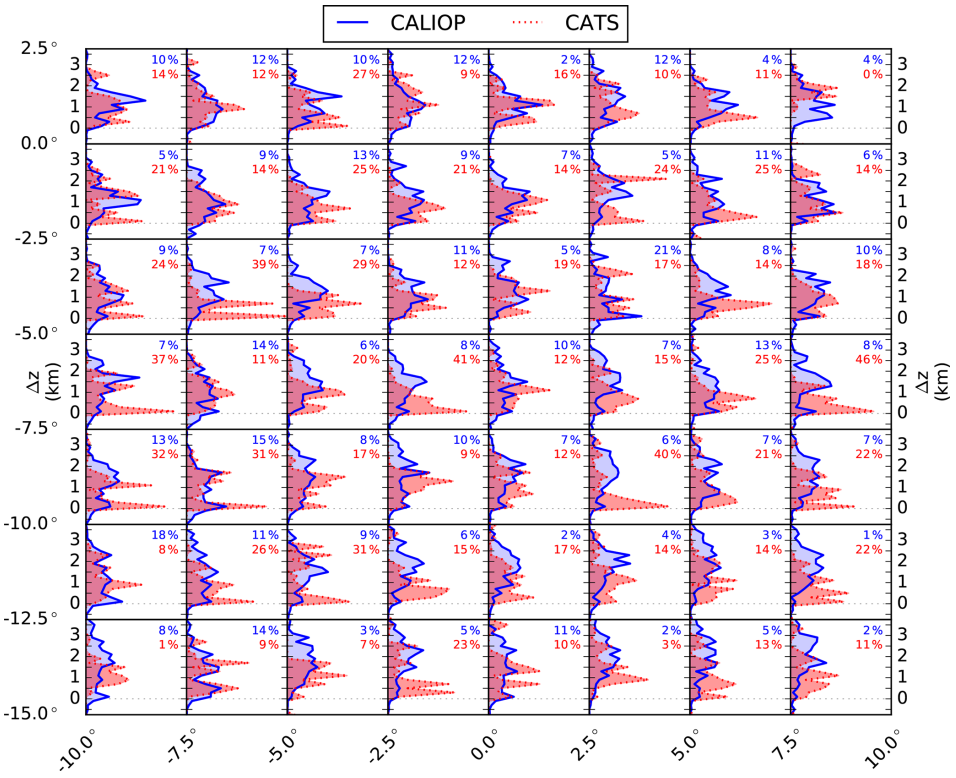

Figure 1. Normalized frequency of occurrence of the gap distance between cloud layer top and aerosol base heights from CALIOP (blue solid line) and CATS (red dotted line) for single layer coincidences of aerosol and cloud in the months of July, August, and September (2007–2016 for CALIOP; 2015–2017 for CATS) over the southeast Atlantic (15° S to 2.5° N, 10° W to 10° E). Layer heights are binned from −1.5 to 5.5 km in 200 m increments, and data in each grid have been normalized to the maximum frequency across the whole study area. The percentage of scenes in which the aerosol layer base is less than 360 m above the cloud-top height is shown in the top right of each subplot for each dataset.

type of experiment aims to understand the importance of correctly retrieving the full geometric extent of the aerosol layer (altitudes of the layer top and base) from a satellite retrieval when the AOD is known; these variables are often provided in combined satellite products such as CCCM (Kato et al., 2010, 2011). This is a known deficiency with retrievals made using wavelengths that are strongly attenuated by biomass burning aerosol such as the 532 nm channel currently used in the CALIOP aerosol products (Rajapakshe et al., 2017). For these experiments the geometric thickness of the aerosol layer is increased from 50 to 500 m with no cloud–aerosol gap and are effectively experiments with variable density of aerosol particles, since with a fixed AOD the aerosol layer mass mixing ratio decreases with the increasing geometric thickness of the layer. The final set of experiments investigates the impact of the cloud–aerosol gap by placing the aerosol layer base from 0 to 500 m above the inversion layer while keeping the geometric thickness and AOD constant. A full list of experiments performed is presented in Table 2. We use one of the experiments, referred to as the base experiment, to provide an initial in-depth analysis of the cloud and radiative response. In the base experiment (hatched experiment in Fig. 2) a 250 m thick absorbing aerosol layer with an AOD of 0.2 is placed directly above the inversion layer.

The SDE is calculated following Johnson et al. (2004) as a residual of the difference in top-of-atmosphere net radiation (F_{TOA}) between the aerosol and no-aerosol simulations, minus the direct radiative effect (DRE):

$$\mathrm{SDE} = F_{\mathrm{TOA,aerosol}} - F_{\mathrm{TOA,no\text{-}aerosol}} - \mathrm{DRE}, \quad (1)$$

where F_{TOA} is calculated using the upward (↑) and downward (↓) fluxes of longwave (LW) and shortwave (SW) radiation:

$$F_{\mathrm{TOA}} = F^{\downarrow}_{\mathrm{TOA,SW}} - \left(F^{\uparrow}_{\mathrm{TOA,SW}} + F^{\uparrow}_{\mathrm{TOA,LW}}\right). \quad (2)$$

DRE is calculated as the difference between F_{TOA} and that obtained in a second diagnostic call to the radiation scheme with the same profiles of liquid water, water vapour, and atmospheric gases but without aerosol. This second call is only performed for the simulations with aerosol present.

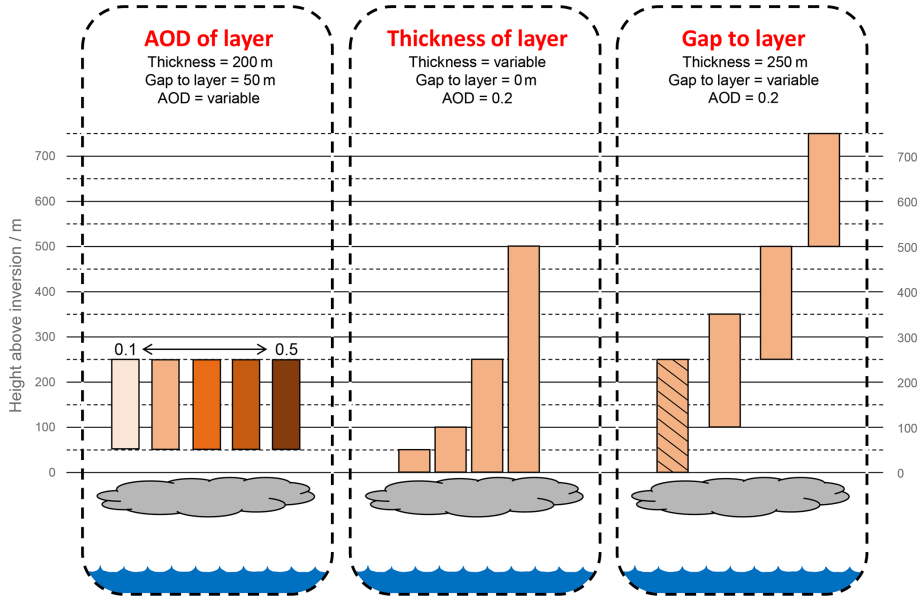

Figure 2. Schematic showing the experiments performed for the aerosol sensitivity simulations. The hatched experiment is named the base experiment and is used to provide an initial analysis of the semi-direct effect in Sect. 3.2. AOD stands for aerosol optical depth and is given at a mid-band wavelength of 505 nm.

Table 2. Breakdown of all experiments performed. AOD stands for aerosol optical depth and is given at a mid-band wavelength of 505 nm. Bold text emphasizes the variable that is being tested in each set of experiments.

Type of experiment	Layer properties		
	Cloud–aerosol gap (m)	Layer thickness (m)	Layer AOD
Variable AOD	50	200	**0.1**
	50	200	**0.2**
	50	200	**0.3**
	50	200	**0.4**
	50	200	**0.5**
Variable thickness	0	**50**	0.2
	0	**100**	0.2
	0	**250**	0.2
	0	**500**	0.2
Variable gap	**0***	250	0.2
	100	250	0.2
	250	250	0.2
	500	250	0.2

* Base experiment used for initial analysis.

3 Results

3.1 No-aerosol experiment

The no-aerosol experiment is initialized and then run for 15 d without the presence of an aerosol layer. The first 5 d are used as a spin-up period that allows the BL to reach a steady state; the following 3 d (days 6, 7, and 8 of the simulation) are shown in Fig. 3.

The no-aerosol experiment produces a cloud-topped BL with strong diurnal variations. During the daytime, cloud-top height decreases and cloud-base height increases, thinning the cloud and producing a diurnal cycle of LWP that reaches a maximum of 60 g m^{-2} at dawn and a minimum of 25 g m^{-2} just after midday (Fig. 3a). The precipitation rate at the surface (not shown) ranges from a maximum of 0.2 mm d^{-1} at night to a minimum of 0.01 mm d^{-1} during the day. For a cloud with an LWP of 60 g m^{-2} this is within the range of observations presented by Abel et al. (2010). The diurnal cycle of the cloud layer can be separated into a growth phase between 14:00 and 06:00 UTC and a decay phase between 07:00 and 13:00 UTC. The growth phase is driven by pronounced buoyancy production during the night (Fig. 3d) from longwave cloud-top cooling and evaporative cooling of entrained air, which drives strong turbulent motion throughout the BL (Fig. 3e). During the daytime, solar heating reduces the buoyancy flux (Fig. 3d) through an offset in the longwave cooling and reduces turbulence throughout the BL (Fig. 3e). This weakens the BL circulation, prevents mixing throughout the BL, and promotes a decoupled state in which the flux of moisture from the surface to the cloud is insufficient to maintain the cloud-base height, as evident from the non-constant BL profiles of θ_l (Fig. 3b) and q_t (Fig. 3c) at 13:00. The weakened flux and solar heating of the cloud drive the lifting condensation level upwards and cause the cloud base to increase with height, producing the decay phase. During the daytime

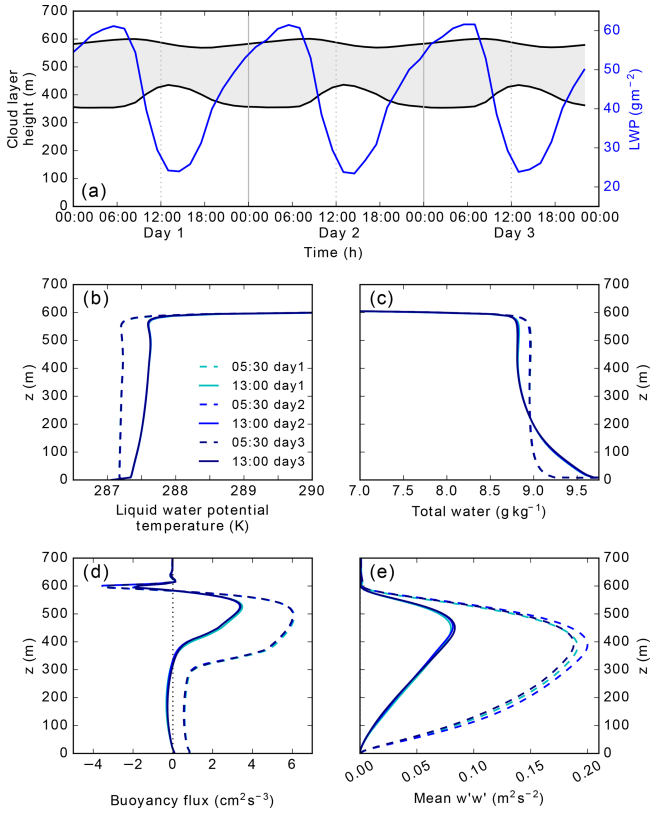

Figure 3. Evolution of domain averaged cloud properties in the no-aerosol simulation including **(a)** cloud top and base (black lines; left axis), liquid water path (blue line; right axis), and vertical profiles taken at 05:30 (dashed lines) and 13:00 (solid lines) on each day for **(b)** liquid water potential temperature, **(c)** total water mass mixing ratio, **(d)** buoyancy flux, and **(e)** the variance in vertical velocity $w'w'$.

weakened BL eddies are unable to "push" against the subsidence at the BL top, which decreases the BL depth and cloud-top height. Due to the different processes that control the cloud-top and cloud-base diurnal variations, the cloud-top height minimum occurs about 2 h after the cloud base reaches its maximum. The cloud layer, LWP, and thermodynamic profiles in Fig. 3a–e show very little change over the 3 d of the simulation and present a stratocumulus deck with a consistent diurnal cycle in a steady state. This provides a suitable simulation to use as a control for the elevated aerosol experiments.

3.2 Cloud response to elevated aerosol layer in the base experiment

We begin with the base experiment (hatched experiment in Fig. 2) for which a 250 m thick absorbing aerosol layer with an AOD of 0.2 is placed directly above the inversion layer. Following a 5 d spin-up period without aerosol, the simulation runs for a further 10 d with the aerosol layer present. The domain-averaged cloud response following the introduction of aerosol is shown in Fig. 4 and compared to the no-aerosol simulation.

The simulations show that the absorbing aerosol drives changes in the diurnal cycle of cloud depth and LWP, predominantly through changes in the cloud-base height. The presence of the absorbing aerosol drives a decrease in cloud-top height (Fig. 4a), which occurs predominantly in the afternoon and evening and is indicative of a decrease in entrainment across the inversion layer. During the initial 2 d the cloud base (Fig. 4a) decreases in altitude $\sim$ 10 m more than the cloud top, resulting in a thicker cloud; however, from day 3 onwards there is less growth of the cloud throughout the evening and early morning, followed by less thinning throughout the day. Compared to the cloud in the presence of no aerosol, the introduction of the absorbing aerosol layer results in relatively less LWP (Fig. 4b) during the growth phase of the cloud and more LWP during the decay phase.

The SDE (Fig. 4d) has a strong diurnal cycle that is directly driven by modifications to the cloud albedo diurnal cycle (Fig. 4c) and shows considerable sensitivity to the LWP response during the cloud decay phase around midday. In the first 3 d the albedo response is positive from mid-morning to the late afternoon. This drives an overall negative daily mean SDE. The length of time with a positive albedo response gets shorter as the simulation progresses, driving an increasingly positive SDE in the morning that cancels out, on a daily mean, the negative SDE in the afternoon. Consequently, the daily mean SDE is negative for the initial 3 d but almost net zero SDE from the fourth day onwards.

The cloud response and SDE are therefore markedly different in the initial phase compared to the steady state that is reached after 6 or 7 d following the introduction of the absorbing aerosol layer. In that steady-state phase the BL depth has decreased by $\sim$ 130 m ($\sim$ 20 %) and the diurnal cycle response in cloud thickness has stabilized. This suggests there are timescales in the response to the introduction of the aerosol layer: a short-term response that can be interpreted as a rapid adjustment of the humidity profile and a longer-term response that can be interpreted as a new equilibrium state for the BL sources of moisture, turbulence, and heat.

This study focuses on the initial response because it is more relevant for real-world understanding as the aerosol perturbation is unlikely to remain constant for several days, and the lifetime of stratocumulus decks is generally on the order of a few days only. However, the steady-state response provides insight into the key drivers behind the BL modifications.

3.2.1 Initial response in the base experiment

The domain-averaged time series of the response in the first 3 d following the introduction of the aerosol layer (days 6, 7, and 8 of the simulation) are shown in Fig. 5. The initial response of the cloud to the elevated aerosol layer is driven by the weakening of the entrainment rate ($w_e = \frac{dz_{cloudtop}}{dt} - w_s$)

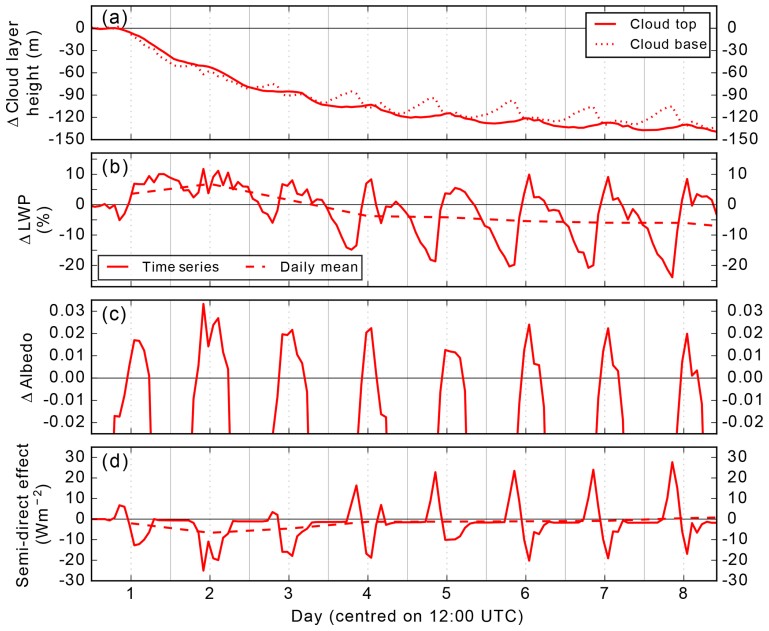

Figure 4. 10 d time series of domain-averaged cloud response to a layer of aerosol directly above the boundary layer inversion with an aerosol optical depth of 0.2 and geometric thickness of 250 m. Plots show the difference between the no-aerosol simulation and the simulation with an elevated aerosol layer for **(a)** cloud-top height (solid line) and cloud-base height (dotted line), **(b)** cloud liquid water path (LWP), **(c)** albedo, and **(d)** the semi-direct effect. Solid lines in **(b)**, **(c)**, and **(d)** show the time series of the response, and dashed lines in **(b)** and **(d)** show the daily mean.

and subsequent increase in the mean RH below cloud, which acts to produce a thicker cloud in the first 2 d. Solar radiation heats the elevated absorbing aerosol layer above the inversion layer. Strengthening of the temperature inversion at the top of the BL drives a weakened w_e (Fig. 5b), which causes the BL depth to decrease (Fig. 5a). Simultaneously, there is an increase in mean RH below cloud (Fig. 5d), which allows the cloud-base height to decrease (Fig. 5a) and the LWP to increase (Fig. 5c); this response continues for the first 2 d, after which the LWP starts to display a diurnal response with a decrease in LWP during the night and an increase in the afternoon. The increase in RH occurs due to the weakened w_e, which reduces the amount of warm dry FT air that is mixed into the BL and allows the sub-cloud layer to maintain a higher RH. The relatively small decrease in potential temperature of ~ 0.1 K (Fig. 5g) suggests that the RH response is driven by an increase in available water vapour. There is little response of the cloud before sunrise, which suggests a weak insulating effect of the aerosol layer on longwave fluxes at the cloud top. This is supported by a lack of systematically weakened cloud-top longwave cooling (Fig. S1 in the Supplement), which would be expected for an increased downwelling longwave flux from the aerosol layer.

The thinner cloud (lower LWP; Fig. 5a) on the morning of the third day is driven by changes to the supply of moisture to the cloud layer. The enhanced RH below cloud and weakened vertical motions (Fig. 5h) drive a strong reduction in surface evaporation as demonstrated by the decrease in latent heat flux (LHF; Fig. 5e), especially during the night. By the end of day 3 the LHF at the surface has been reduced by 20 % and the total water path (TWP) of the BL (Fig. 5f) has been reduced by 10 %. During the night when the BL is well mixed this reduction in TWP prevents the cloud from developing to the same extent as in the no-aerosol simulation, resulting in a thinner cloud when the sun rises. This process is amplified by the reduced BL dynamics, which will weaken the flux of moisture from the sub-cloud region to the cloud.

The thicker cloud (enhanced LWP; Fig. 5a) on the afternoon of the third day is driven by relatively stronger coupling with the surface moisture fluxes at midday, which produces a slightly thicker cloud and a negative SDE (Fig. 5i). Under no-aerosol conditions, shortwave absorption by the cloud stabilizes the cloud layer during the day, which results in a degree of decoupling between the surface layer and cloud base (Fig. 3). When an elevated absorbing aerosol layer is present, the decrease in cloud layer height, following the BL depth decrease, allows for better coupling to the surface (see Fig. S2 in the Supplement), which becomes increasingly important around midday when the BL dynamics are weakest (Fig. 5h). The enhanced source of moisture to the cloud base, along with weakened entrainment of dry FT air, prevents the cloud from thinning to the same extent. Although the change in LWP is only 2–3 g m^{-2}, this amounts to a 10 % increase, which helps drive a strong negative SDE at midday and early afternoon.

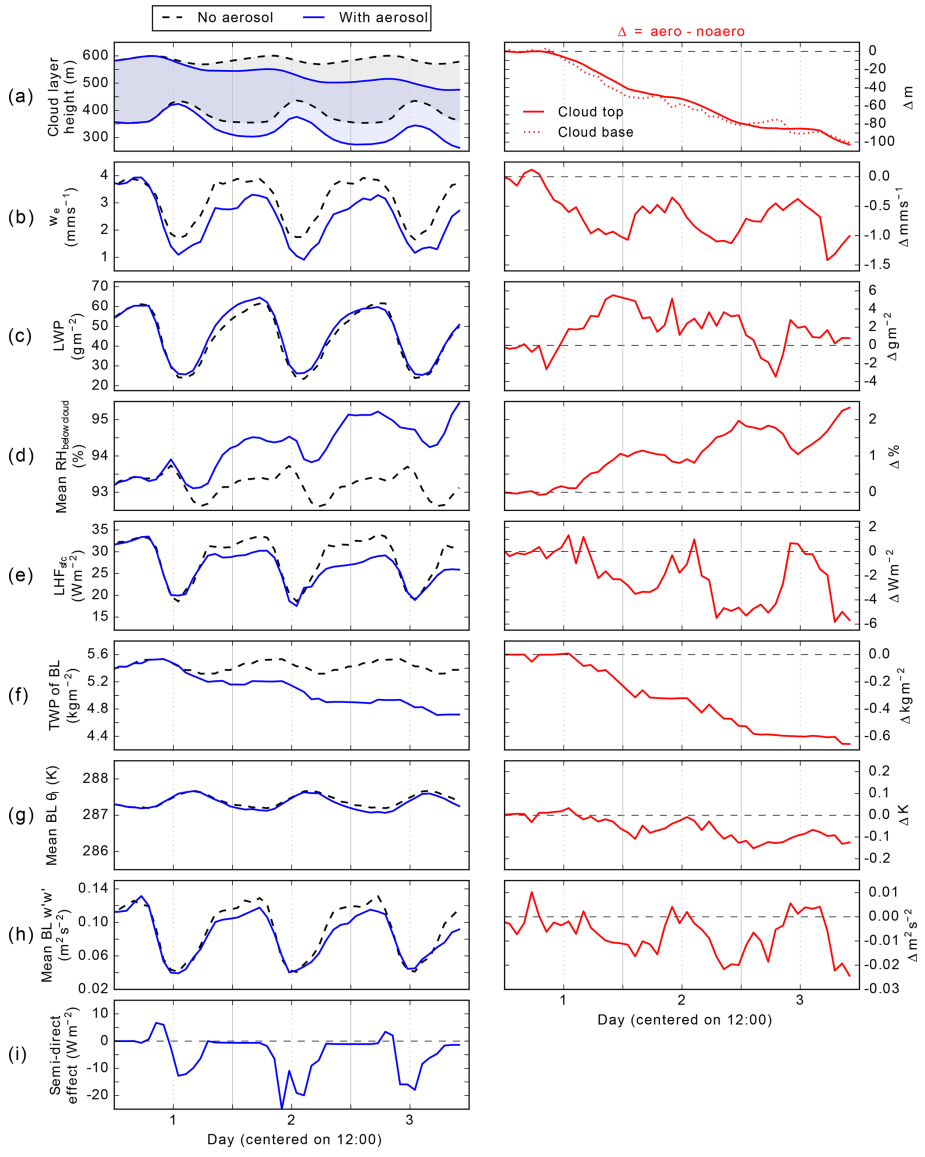

Figure 5. 3 d time series showing the initial domain-averaged cloud response to a layer of absorbing aerosol in the base experiment (0 m cloud–aerosol gap, 250 m thick layer, and AOD of 0.2). In the first column the black dashed lines refer to the control experiment (no-aerosol) and solid blue lines to the experiments with the aerosol layer present. The second column shows the cloud response (red solid line). The plots show **(a)** the altitude of the cloud base and top, **(b)** the entrainment rate w_e, **(c)** the liquid water path (LWP), **(d)** the mean relative humidity (RH) between the ocean surface and the cloud base, **(e)** the latent heat flux (LHF) from the surface, **(f)** the total water path (TWP) of the boundary layer (BL), **(g)** the mean liquid water potential temperature (θ_l) of the BL, **(h)** the mean BL vertical velocity variance ($w'w'$), and **(i)** the semi-direct effect.

The analysis of the initial cloud response shows that the first 2 d are characterized by a general thickening of the cloud driven by the reduction in w_e across the temperature inversion and subsequent enhanced RH profile below cloud via an increase in water vapour. The weakened w_e, BL dynamics, and moisture flux from the surface begin to dry the BL, resulting in less cloud growth overnight, whilst the lower cloud base enhances coupling to the surface moisture fluxes during the middle of the day, and less cloud decay.

3.2.2 Steady-state response in the base experiment

The final 3 d of the 15 d base experiment provide a mean diurnal cycle of the cloud response. Although aerosol layers do not persist above stratocumulus decks for so long in reality, the steady-state response provides insight into the key drivers behind the BL modifications. The steady-state response of the cloud to the elevated aerosol layer, shown in Fig. 6, shows strong similarities to the third day of the initial response: the growth phase of the cloud (Fig. 6b) is weakened, producing

a thinner cloud in the morning, and the decay phase of the cloud (Fig. 6b) is weakened, producing a thicker cloud in the early afternoon. This modification to the diurnal cycle of the cloud is driven by an increased coupling between the surface moisture flux and cloud base during the daytime (see Fig. S2 in the Supplement) and an overall decrease in TWP of the BL with weakened dynamics overnight. The decrease in cloud layer height allows for better mixing beneath the cloud base, which enhances the evaporation of moisture from the surface between 09:00 and 15:00 (Fig. 6d); this is evident from the weakened diurnal cycle in mean RH below cloud (Fig. 6c), which usually occurs due to poor mixing, and the strengthened BL dynamics at midday (Fig. 6g). The small response in the mean BL potential temperature of -0.2 K (Fig. 6f) strengthens the hypothesis that the RH response below cloud is driven by changes in available water vapour rather than the decrease in temperature, although it is worth noting that this decrease in temperature will act to slightly increase the RH.

The weakened cloud growth phase overnight occurs due to a 15 % reduction in TWP of the BL (Fig. 6e) and a reduction in mean BL vertical motions overnight of ~ 20 %, indicated by the mean BL vertical velocity variance ($w'w'$) in Fig. 6g. The reduction in w_e (Fig. 6a) and subsequent changes to below-cloud water vapour set up a positive feedback mechanism with BL dynamics: vertical motions in the BL are considerably weakened throughout the night and slightly strengthened at midday. Although there is a decrease in LWP there is no systematic impact on the cloud-top longwave cooling due to its weak sensitivity to LWP above 50 g m^{-2} (van der Dussen et al., 2013; Garrett and Zhao, 2006). The weakened BL circulation is therefore due to a reduction in entrainment. The mixing of dry air into the cloud layer results in evaporation and a cooling that generates buoyancy; a reduction in entrainment therefore weakens cloud-top buoyancy production. These combined changes result in reduced vertical motions within the BL, which reduce surface evaporation, cloud LWP, and buoyancy production from condensation at the cloud base, which allow the reduced vertical motions to persist. A partial offset to this process occurs during midday when stronger coupling to the surface results in enhanced transport of water vapour to the cloud base.

The steady-state response establishes itself by the third day of the simulation. The daily mean steady-state SDE (Fig. 6h) results from a balance between the degree to which the BL TWP has decreased, producing a positive SDE in the morning, and the degree to which the midday coupling is enhanced, producing a negative SDE in the afternoon. In both cases modifications to BL depth, and thus w_e, play a significant role in cloud response and SDE.

3.3 Sensitivity of initial response to aerosol layer properties

Figure 7 shows time series for the aerosol layer sensitivity experiments. In this analysis the inversion strength $\Delta\theta_l$ is determined between altitudes z_{upper} and z_{lower}. The value of z_{upper} is the topmost altitude at which the absolute gradient $\left|\frac{d\theta_l}{dz}\right|$ is 25 % of its maximum, and z_{lower} is the lowermost altitude at which $\left|\frac{d\theta_l}{dz}\right|$ is 2.5 % of its maximum. The upper threshold is determined at a higher percentage of $\left|\frac{d\theta_l}{dz}\right|$ than the lower threshold to limit spurious values occurring from aerosol layers close to the inversion layer that impact θ_l.

3.3.1 Cloud response

The majority of experiments show a positive spike in SDE (Fig. 7d, i, and n) just before midday on the first day. This occurs due to the lag time in response between the direct impact on the cloud from changes to w_e and the increase in sub-cloud RH. Figure S1 in the Supplement focuses on the response in the initial 24 h. The positive SDE is driven by the decrease in LWP caused by an increase in cloud-base height (Figs. 5a and S1a) without a corresponding change in cloud-top height. The decrease in w_e weakens buoyancy production throughout the cloud layer (Fig. S1c), which drives a reduced moisture flux within the cloud and to the cloud base (Fig. S1d). As the day progresses the continued reduction of w_e results in an increase in mean below-cloud RH and a recovery of, or increase in, the LWP. This explains why stronger perturbations to the entrainment rate on the first day (such as when the layer is close to the cloud) result in a quicker recovery of the LWP (Fig. 7c, h, and m). This result suggests that the specific timing of the incoming aerosol plume may play a role in the cloud response and SDE on the first day.

Geometrically thinner aerosol layers equate, for a given AOD, to a greater aerosol mass mixing ratio and therefore stronger heating. This results in a stronger inversion layer (Fig. 7a) and stronger modification to the LWP response (Fig. 7c) and SDE (Fig. 7d), especially on the first day. This stronger inversion layer weakens w_e and decreases BL depth (Fig. 7b). For the two thinnest layers the cloud-top height decreases at a faster rate during the day than at night, which correlates with the peak heat perturbation. For thicker layers the heat perturbation extends further into the night; this corresponds with the delay in time for the heating towards the top of the layer to reach the inversion layer and drives a steadier reduction in BL depth when compared to the thinner layers. By the third day the BL has started to adjust and less dependence on aerosol layer thickness is apparent; however, the thinner layers cause the BL to dry out at a quicker rate, thus producing a stronger positive SDE on the morning of the third day.

Increasing the cloud–aerosol gap leads to a weaker and increasingly delayed cloud-top height (Fig. 7g) and LWP response (Fig. 7h) driven by changes in peak strengthening of the inversion (Fig. 7f); this is most pronounced in the first 2 d. Only aerosol layers directly above the inversion trig-

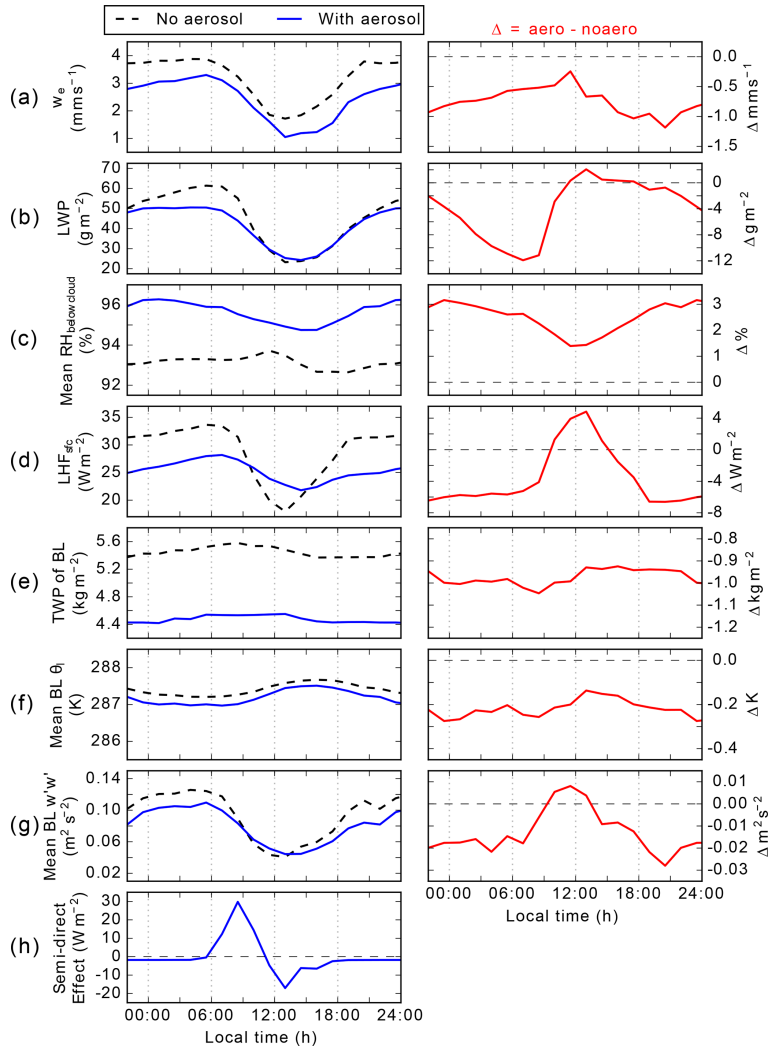

Figure 6. Domain-averaged cloud response to a layer of absorbing aerosol directly above the inversion in the base experiment (0 m cloud–aerosol gap, 250 m thick layer, and AOD of 0.2) for the mean diurnal cycle using the final 3 d of the 15 d simulation. In the first column the black dashed lines refer to the control experiment (no-aerosol) and solid blue lines to the experiments with the aerosol layer present. The second column shows the cloud response (red solid line). The plots show **(a)** the entrainment rate w_e, **(b)** the liquid water path (LWP), **(c)** the mean relative humidity (RH) between the ocean surface and cloud base, **(d)** the latent heat flux (LHF) from the surface, **(e)** the total water path (TWP) of the boundary layer (BL), **(f)** the mean liquid water potential temperature (θ_l) of the BL, **(g)** the mean BL vertical velocity variance ($w'w'$), and **(h)** the semi-direct effect.

ger a considerable cloud response on the first day because of the relatively rapid strengthening of the inversion layer and weakening of w_e, which forces the cloud top downwards more rapidly than the RH profile can adjust, resulting in a deeper cloud base. On the second day a cloud response is seen with gaps up to 100 m, and by the third day all gaps lead to a response in cloud LWP. The delay in response is driven by the delay in the inversion layer strengthening. In the free troposphere the advection of the heat perturbation is driven by subsidence; therefore, greater cloud–aerosol gaps require more time for the heat perturbation to reach the cloud top. Simultaneously, longwave cooling acts to weaken the heat perturbation throughout its advection, which drives a relatively weaker strengthening of the temperature inversion as the cloud–aerosol gap increases.

The initial cloud-top response (Fig. 7l) displays a strong dependence on the AOD of the aerosol layer throughout the 3 d, with greater AOD resulting in a greater response. As with geometric layer thickness, larger AODs absorb more radiation and drive a stronger heat perturbation and inversion strength (Fig. 7k). So larger AODs result in a thicker cloud and a more negative SDE. On the third day layers with the largest AODs, which have had the greatest impact on cloud-top height and w_e, exhibit a considerably thinner cloud, driving an increasingly positive SDE in the morning.

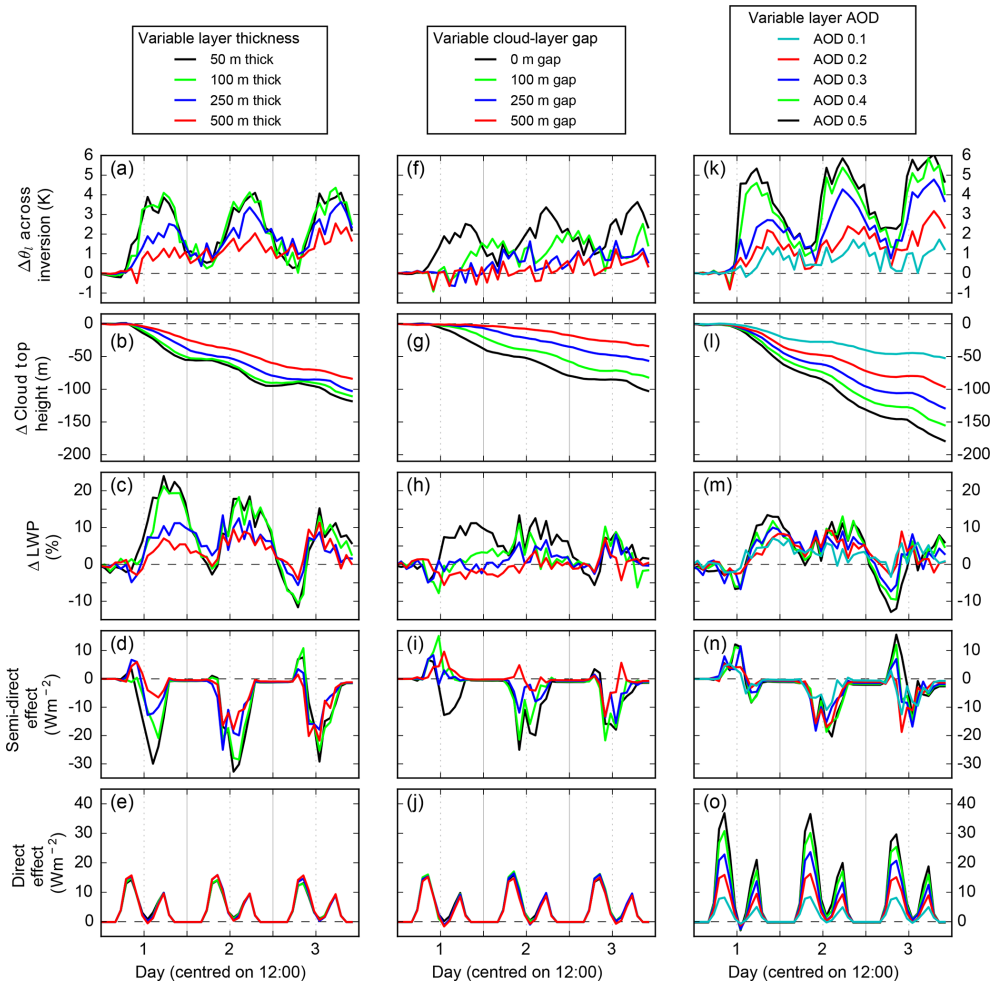

Figure 7. 3 d time series showing the sensitivity of the initial cloud response (difference between the no-aerosol simulation and the simulation with an elevated aerosol layer) to the properties of the elevated absorbing aerosol layer. The three columns correspond to experiments in which systematic changes have been made to the aerosol layer thickness **(a–e)**, cloud–aerosol gap **(f–j)**, and aerosol layer AOD **(k–o)**.

In summary, the layer sensitivity experiments show that on the first day the initial response is for the cloud top to drop quicker than the cloud base, resulting in a thinner cloud and a positive SDE in the morning, the magnitude of which is primarily driven by the proximity of the aerosol layer to the cloud top. With no gap between the inversion at the cloud top and aerosol layer, the afternoon of the first day is characterized by a thicker cloud and negative SDE, which increases in magnitude for stronger heat perturbations. The second day is generally characterized by an increase in the LWP at midday, which drives a negative SDE and is dependent on the location and properties of the aerosol layer. By the third day a consistent pattern occurs: the cloud is consistently thinner in the morning and thicker at midday, the magnitude of which is dependent on the strength of the perturbation.

3.3.2 Radiative response

Figure 8 shows time series of the daily mean radiative effects for the layer sensitivity experiments. The immediate radiative response following the introduction of the absorbing aerosol layer is primarily dependent on the distance between the inversion layer and aerosol layer base. When there is no cloud–aerosol gap the increase in LWP results in a negative SDE; thinner layers and larger AODs increase the inversion layer strengthening and drive a stronger negative SDE on the first day. When any cloud–aerosol gap is present there is little LWP response on the first day due to the delayed inversion layer strengthening; however, all experiments with a gap present are characterized by a small positive SDE. For the experiments with a 50 m gap (variable AOD experiments) the delay is short enough that there is an increase in LWP in the evening of the first day (Fig. 8i).

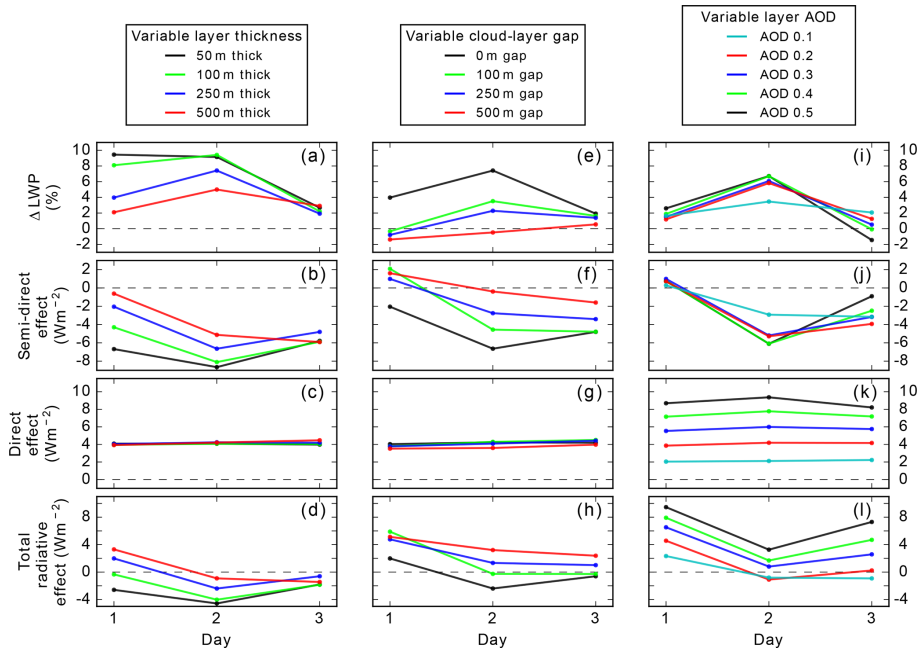

Figure 8. Daily mean radiative impact on the elevated aerosol layer properties over the initial 3 d following the introduction of the aerosol layer for systematic changes to **(a–d)** aerosol layer thickness, **(e–h)** cloud–aerosol gap, and **(i–l)** aerosol optical depth of layer.

On the second and third day the SDE is negative for all experiments; the magnitude of the SDE increases for thinner layers closer to the inversion layer. When a cloud–aerosol gap is present the AOD tends to have little impact on the magnitude of the SDE. The rate at which the BL moisture content decreases, itself a factor of how strongly w_e is perturbed, results in variations in which day the peak SDE occurs. In experiments with gaps smaller than 100 m the maximum SDE is reached on the second day, whereas for gaps larger than or equal to 100 m the maximum occurs on the third day. In all experiments the third day is characterized by a decrease in the daily mean LWP response, which is primarily driven by less cloud growth overnight and in the morning (see Fig. 7c, h, and m) and becomes more pronounced as the temperature inversion strengthens. The thinner cloud in the morning helps to shift the daily mean SDE towards zero.

The properties of the aerosol layer have a considerable impact on the total radiative effect, calculated as the sum of the DRE and SDE (Fig. 8d, h, and l). Generally, the SDE acts to counteract the positive DRE and in some cases results in an overall negative total radiative effect. In all experiments the total radiative effect is sensitive to the layer properties, whereas DRE is only sensitive to the layer AOD. In many instances the SDE is greater in magnitude than the DRE, with the second day constituting the period of time with the greatest impact. The relative insensitivity of the SDE to changes in AOD suggests that layers with a moderate AOD (~ 0.2) may have the strongest overall radiative impact due to the relatively low DRE; however, the behaviour may change for increasing gaps.

The results of the experiments are summarized in Table 3 with the daily mean SDE alongside the means for the periods before and after midday. The daily mean SDE is only consistently negative throughout the 3 d when there is no cloud–aerosol gap. This result is consistent with Johnson et al. (2004), who similarly found a negative SDE for a ~ 1000 m layer of absorbing aerosol (AOD of 0.2, SSA of 0.88) directly above the inversion layer. Johnson et al. (2004) calculated a mean SDE of $-9.5\,\mathrm{W\,m^{-2}}$ and a mean DRE of $10\,\mathrm{W\,m^{-2}}$. These magnitudes are greater than in this study but similarly show that the SDE is of approximately equal magnitude to the DRE and of opposite signs. Our results also show that geometrically thin, but optically thick, aerosol layers will have a stronger forcing than a thicker layer with the same AOD due to a stronger localized heat perturbation; this effect is most prominent on the first day. When a gap to the aerosol layer base is present, as is predominantly observed (Fig. 1), our results show that the short-term SDE is likely to be weakly positive but then becomes negative once the BL has been mixed, which usually occurs during the first night when BL turbulence peaks, highlighting a sensitivity to the specific arrival timing of the incoming plume. On the second and third day the magnitude of the SDE then depends on the AOD, cloud–aerosol gap, and aerosol layer thickness.

Table 3 highlights the diurnal variations in the SDE. The SDE is generally more negative after midday but that contrast varies with aerosol layer properties. Geometrically thin, optically thick layers directly above the inversion layer display the strongest contrast with the daily mean SDE dominated by the mean after midday. When a gap is present there is less

Table 3. Mean semi-direct effect ($W\,m^{-2}$) for each of the aerosol experiments shown in Fig. 2 and Table 2. Mean values are presented for each day (daily) between 00:00 and 12:00 (morning) and between 12:00 and 24:00 (afternoon). Bold text emphasizes the variable that is being tested in each set of experiments.

Type of	gap	dz	AOD	Day 1			Day 2			Day 3		
experiment				Daily	Morning	Afternoon	Daily	Morning	Afternoon	Daily	Morning	Afternoon
Variable	**0**	250	0.2	−2	1	−5	−7	−6	−7	−5	−4	−6
gap	**100**	250	0.2	2	4	0.4	−5	−5	−4	−5	−5	−5
	250	250	0.2	1	2	0.3	−3	−3	−3	−3	−3	−4
	500	250	0.2	2	1	2	−0.4	1	−1	−2	−3	−0.5
Variable	0	**50**	0.2	−7	−2	−12	−9	−5	−13	−6	−2	−10
thickness	0	**100**	0.2	−4	−1	−8	−8	−5	−11	−6	−2	−10
	0	**250**	0.2	−2	1	−5	−7	−6	−7	−5	−4	−6
	0	**500**	0.2	−1	2	−3	−5	−4	−6	−6	−5	−7
Variable	50	200	**0.1**	0.3	2	−1	−3	−3	−3	−3	−2	−4
AOD	50	200	**0.2**	1	2	−0.1	−5	−5	−6	−4	−4	−4
	50	200	**0.3**	1	2	−0.1	−5	−5	−5	−3	−1	−5
	50	200	**0.4**	1	2	−1	−6	−4	−8	−2	−0.4	−5
	50	200	**0.5**	1	3	−1	−6	−4	−8	−1	3	−5

contrast and both time periods are generally representative of the daily mean, until the BL begins to dry out significantly in the high AOD experiments. These results demonstrate that there are often strong diurnal variations in the SDE that are sensitive to the aerosol layer properties and suggest that observations of the SDE made within a small window of time, e.g. those from polar-orbiting satellites, may be unrepresentative of the daily mean SDE.

3.4 Sensitivity to boundary layer and cloud properties

This section investigates the robustness of the results and conclusions from Sect. 3.3. The parameter space considered in this section includes previous LEM studies, such as Hill and Dobbie (2008) and Johnson et al. (2004), and the range of environmental forcings observed within marine stratocumulus regions.

The first set of sensitivities focuses on the model setup and includes no precipitation from the cloud (noRain) and an enhanced large-scale advective heat tendency of $-0.5\,K\,d^{-1}$ (05cool).

- In the noRain setup the production of precipitation is switched off. Stratocumulus clouds frequently produce precipitation in the form of drizzle (Leon et al., 2009), yet studies often simplify simulations by focusing on non-precipitating stratocumulus (e.g. Hill and Dobbie, 2008; Johnson et al., 2004). Precipitation redistributes moisture from the cloud layer to the sub-cloud layer, promoting BL stability and acting to reduce BL dynamics and cloud LWP (Ackerman et al., 2009).

- In the 05cool sensitivity, the magnitude of the large-scale advective heat tendency is increased from -0.1 to $-0.5\,K\,d^{-1}$. That parameter accounts for the equatorward transport of the large-scale air mass and is negative in subtropical marine regions. This value can be estimated using large-scale reanalyses (e.g. Johnson et al., 2004) or used as a balancing term to prevent subsidence heating and represents a degree of variability in LES setups.

The second set of sensitivities focuses on properties of the BL that may impact the diurnal cycle and maintenance of the cloud.

- In the SST − 1K and SST+1K setups, SST is decreased and increased by 1 K, respectively, while keeping the BL depth at 600 m. Stratocumulus decks in the Atlantic and Pacific oceans are observed over a wide range of sea surface temperatures (Sandu and Stevens, 2011; Wood, 2012). As the SST increases the differential temperature across the surface–air boundary increases, resulting in more pronounced surface moisture and sensible heat fluxes.

- The wetFT setup increases the mass mixing ratio of water vapour in the FT by $+0.4\,g\,kg^{-1}$ to assess the impact of the water vapour content of the entrained air on the SDE. Trajectory analyses from the Pacific and Atlantic oceans by Sandu et al. (2010) show that the mass mixing ratio of water vapour in the FT varies spatially and temporally, ranging from 1.0 to $7.5\,g\,kg^{-1}$ at 700 hPa; this result is supported by in situ data summarized by Albrecht et al. (1995).

- The 800 m and 1000 m setups increase the height of the temperature inversion by 200 and 400 m, respectively, by changing the large-scale divergence rate and

initial profiles of θ_l and q_t, while keeping SST constant at 287.2 K. Observations show that cloud-top heights in regions of semi-permanent stratocumulus coverage (southeast Atlantic, southeast Pacific, and northeast Pacific) typically range from ~ 500 to ~ 1500 m (Muhlbauer et al., 2014; Painemal et al., 2014; Wyant et al., 2010) with variations driven by SST and subsidence.

To isolate the cloud response due to the aerosol layer, the cloud sensitivity experiments are initialized using profiles that produce an approximately constant stratocumulus cloud layer at the top of the BL following the method described in Sect. 2.2.

Table 4 shows the resulting initial profiles and large-scale divergence rates for each setup. The same sets of experiments from Sect. 3.3 are performed for each setup, along with a simulation without aerosol to calculate the BL response to the aerosol perturbation. The daily mean SDE on day 2 following the introduction of the absorbing aerosol layer (day 7 of the simulation) is shown in Table 5 for each setup and aerosol experiment. For the control setup the SDE values are the same as shown in Fig. 8.

3.4.1 Sensitivity to model setup

Comparing the no-aerosol simulations, the removal of precipitation results in stronger BL dynamics and a greater peak in LWP ($+15\,\mathrm{g\,m^{-2}}$) than the control setup. The noRain setup is characterized by a consistent increase in the magnitude of the SDE by $1\,\mathrm{W\,m^{-2}}$ when a cloud–aerosol gap is present and up to $3\,\mathrm{W\,m^{-2}}$ when there is no gap. In the control setup the presence of the aerosol layer increases cloud LWP, which is partially offset by an increase in precipitation. In the noRain setup that partial offset is not allowed, resulting in a relatively enhanced LWP response and SDE.

When compared to the control setup, increasing the cooling rate of the large-scale advective heat tendency results in stronger BL dynamics, enhanced cloud-top entrainment of warm dry air, and enhanced surface LHF (which acts as a feedback to enhanced entrainment). As the processes maintaining the cloud layer become more important, they become more sensitive to perturbations. Therefore, when the aerosol layer is present in the 05cool setup, the responses of w_e, LHF, and below-cloud moisture flux are stronger than in the control setup, and the simulations are characterized by a quicker decrease in the TWP of the BL. However, this only becomes prominent on the third day and results in little difference from the control setup over the first 2 d.

3.4.2 Sensitivity to BL properties

In the no-aerosol simulations warmer SST drives an enhanced below-cloud moisture flux but a lower LWP due to an increase in BL temperature. The warmer BL also leads to stronger in-cloud buoyancy production. When the aerosol layer is present the LWP response increases with SST, driving a stronger negative SDE in all experiments. The cloud response is particularly sensitive to SST when the aerosol layer is near the cloud top. As discussed in Sect. 3.2, the initial response from the weakened w_e, and subsequently enhanced RH, occurs quicker than the moisture source from the surface can readjust to. The reductions in w_e and BL depth are equivalent for all SST, but the greater flux of moisture from warmer SST results in a greater increase in mean q_t and RH perturbation, leading to a lower cloud base, thicker cloud, and tending to push the SDE towards a more negative daily mean. The sensitivity of the radiative response is driven by both the SST and the perturbation to w_e; therefore, stronger heat perturbations closer to the cloud top result in a more pronounced sensitivity to SST.

The no-aerosol simulation for the wetFT setup is characterized by an LWP $+5\,\mathrm{g\,m^{-2}}$ greater than the control setup, with slightly weaker surface evaporation. This increase in LWP is caused by entrainment of slightly moister FT air in the wetFT setup, allowing the BL to maintain a greater mean RH. The mixing of entrained air has a smaller impact on the cloud humidity, which then does not need to be balanced as strongly from a source at the surface. When the aerosol layer is present the weakened w_e therefore has a smaller impact on the RH response of the BL, which results in a smaller SDE. This setup shows that the degree to which the entrained air impacts the cloud plays an important role in the strength of the SDE: very dry FT air will play a more important role in reducing RH so that a perturbation to w_e will have a greater impact on the cloud response.

3.4.3 Sensitivity to BL depth

As the BL depth increases its temperature increases and the TWP of the BL decreases. Figure 9 shows the profiles of θ_l and q_t for the three setups (control, 800 m, 1000 m) during the time of the strongest (05:30) and weakest (13:00) BL dynamics. During the period with the weakest dynamics the degree of coupling, or mixing, between the sub-cloud and cloud layers is weakened. This reduces the flux of water vapour from the surface layer to the cloud, resulting in an accumulation of water vapour close to the surface (Fig. 9b). That redistribution becomes more pronounced as the BL depth increases, increasing BL decoupling.

Increasing the BL depth has a dramatic effect on the sign and magnitude of the SDE shown in Table 5. The SDE switches sign from negative for a 600 m deep BL in the control setup to positive in the 800 m and 1000 m setups. The SDE in the 800 m setup is roughly of equal magnitude to the control, but the 1000 m setup is considerably greater in magnitude, peaking at $+26\,\mathrm{W\,m^{-2}}$. Responses for the base experiment shown in Fig. 10 help to illustrate why the BL depth has such a strong impact on the SDE. In all setups the cloud-top height decreases by ~ 100 m over the 3 d (Fig. 10a, g, and m), driven by similar changes in w_e (Fig. 10e, k, and q); however, the response in cloud-base height depends on the

Table 4. Initial profiles of liquid water potential temperature (θ_l; K) and total liquid mass mixing ratio (q_t; g kg^{-1}) against altitude (z in metres) for each cloud sensitivity setup. Values in parentheses indicate the large-scale divergence rate (D; s^{-1}) used for each setup. All setups result in a stable stratocumulus cloud deck at the top of the boundary layer.

z	noRain (5.4×10^{-6})		05cool (6.2×10^{-6})		SST−1K (4.75×10^{-6})		SST+1K (5.75×10^{-6})		wetFT (5.25×10^{-6})		800 m (4.0×10^{-6})			1000 m (2.75×10^{-6})		
	θ_l	q_t	θ_l	q_t	θ_l	q_t	θ_l	q_t	θ_l	q_t	z	θ_l	q_t	z	θ_l	q_t
0	287.5	9.0	287.3	9.0	286.5	8.6	288.3	9.4	287.3	9.0	0	287.3	9.0	0	287.3	9.0
600	287.5	9.0	287.3	9.0	286.5	8.6	288.3	9.4	287.3	9.0	800	287.3	9.0	1000	287.3	9.0
601	297.0	5.5	296.0	5.5	296.0	5.5	297.2	5.5	297.0	5.9	801	297.0	5.9	1001	297.0	5.9
750	300.0	5.5	299.0	5.5	300.0	5.5	300.0	5.5	299.5	5.9	900	299.5	5.9	1100	299.5	5.9
1000	301.7	5.5	300.3	5.5	301.7	5.5	301.7	5.5	301.5	5.9	1200	301.5	5.9	1300	301.5	5.9
1500	303.2	5.5	301.5	5.5	303.2	5.5	303.2	5.5	302.6	5.9	1700	302.6	5.9	1900	302.6	5.9
2600	304.0	5.5	302.8	5.5	304.0	5.5	304.0	5.5	303.8	5.9	2600	303.8	5.9	2600	303.8	5.9

Table 5. Daily mean semi-direct radiative effect for the second day following the introduction of the absorbing aerosol layer for control and cloud sensitivity setups. All values are as a daily mean (W m^{-2}). Layer properties include the cloud–aerosol gap ("gap", in metres), the geometric thickness of the layer ("dz", in metres), and the aerosol optical depth (AOD) of the layer given at a mid-band wavelength of 505 nm. Bold text emphasizes the variable that is being tested in each set of experiments.

Type of experiment	gap	dz	AOD	control	noRain	05cool	SST−1K	SST+1K	wetFT	800 m	1000 m
Variable gap	**0**	250	0.2	−7	−8	−5	−5	−8	−6	4	17
	100	250	0.2	−5	−6	−5	−3	−7	−3	6	10
	250	250	0.2	−3	−4	−4	−1	−5	−2	6	6
	500	250	0.2	0	−1	−2	1	0	0	4	2
Variable thickness	0	**50**	0.2	−9	−12	−7	−7	−13	−8	0	18
	0	**100**	0.2	−8	−10	−7	−5	−11	−7	2	20
	0	**250**	0.2	−7	−8	−5	−5	−8	−6	4	17
	0	**500**	0.2	−5	−7	−5	−2	−8	−5	5	11
Variable AOD	50	200	**0.1**	−3	−5	−3	−1	−3	−3	6	7
	50	200	**0.2**	−5	−7	−4	−3	−6	−5	5	15
	50	200	**0.3**	−5	−9	−4	−4	−8	−6	5	22
	50	200	**0.4**	−6	−9	−5	−4	−10	−5	6	25
	50	200	**0.5**	−6	−7	−5	−4	−10	−5	5	26

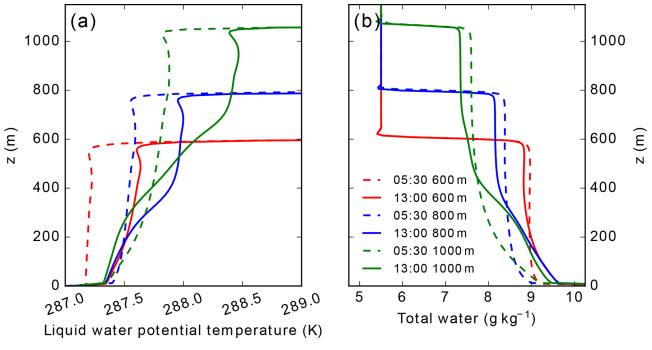

Figure 9. Vertical profiles of **(a)** liquid water potential temperature and **(b)** total water mass mixing ratio taken at 05:30 (dashed lines) and 13:00 (solid lines) on day 1 (after spin-up) for the no-aerosol simulations.

simulation and accounts for the variation in LWP response (Fig. 10b, h, and n). In the 1000 m setup (Fig. 10m) the cloud base decreases less than the cloud top throughout the time series, driving a consistently reduced LWP.

As shown in Fig. 9 the degree of decoupling between the sub-cloud and cloud layers increases with BL depth. The diurnal cycle of the sub-cloud RH for the three setups (Fig. 10d, j, and p) shows that longer periods of decoupling occur as the BL depth increases (elevated and prolonged mean sub-cloud RH corresponds to a poorly mixed BL). In both the control and 800 m setups the BL is reasonably well mixed throughout the day. The presence of the aerosol layer enhances the midday coupling and weakens the cloud decay phase, producing a thicker cloud in the afternoon. However, for the 1000 m setup the lowering of the cloud layer is not sufficient to overcome the decoupling that occurs; therefore, there is no additional flux of moisture at midday and the cloud does

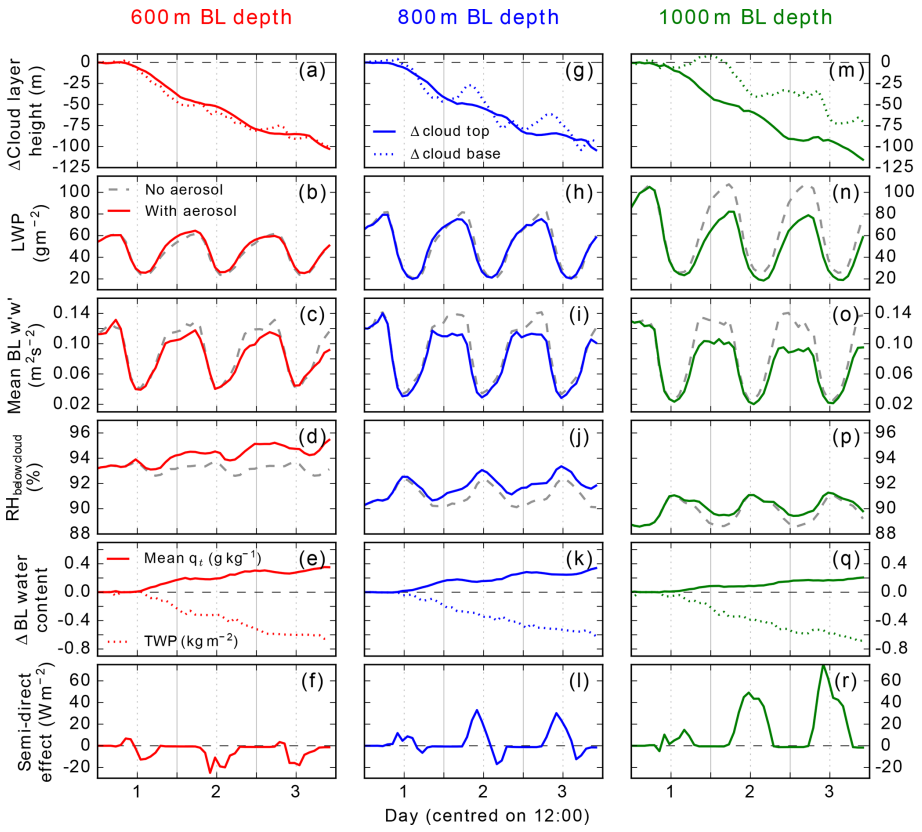

Figure 10. 3 d time series showing the initial response of the cloud to a 250 m thick layer of aerosol directly above the inversion with an aerosol optical depth of 0.2 from the **(a)–(f)** control setup with a boundary layer depth of 600 m, **(g)–(l)** 800 m setup, and **(m)–(r)** 1000 m setup. From the top to bottom row, panels show the altitude of the cloud base and top, the liquid water path (LWP), the mean boundary layer (BL) vertical velocity variance ($w'w'$), the mean relative humidity (RH) between the ocean surface and the cloud base, changes to the BL water content as the mean total water content q_t and the total water path (TWP), and the semi-direct effect.

not thicken, producing a positive SDE in the afternoon. As the BL deepens overnight, the dynamics become increasingly sensitive to the elevated absorbing aerosol layer (Fig. 10c, i, and o). The result is a more pronounced decrease in the cloud growth phase overnight and a thinner cloud in the morning. The 800 m and 1000 m setups produce a strong positive SDE in the morning from day 2 onwards (Fig. 10l and r), which dominates the daily mean SDE (Table 5). As described in Sect. 3.2.2, reductions in w_e and below-cloud moisture fluxes set up a feedback mechanism that decreases the BL dynamics. As the BL deepens this mechanism occurs more rapidly and may be further enhanced by reduced cloud-top longwave cooling that occurs when the LWP is sufficiently reduced. The reduction by $\sim 30\,\mathrm{g\,m^{-2}}$ of the LWP in the 1000 m setup is a large enough perturbation to reduce the longwave cloud-top cooling by $\sim 40\,\%$ and decrease buoyancy production.

These results explain the different aerosol layer sensitivities shown in Table 5. In all setups the enhanced temperature inversion weakens w_e and the mixing of warm, dry FT air into the cloud layer and enhances midday coupling. For the control setup there is little impact on BL dynamics, so the cloud becomes thicker due to enhanced sources of moisture; as the temperature inversion strengthens this response increases. As the BL deepens the BL dynamics are increasingly weakened, driving a reduction in sub-cloud sources of moisture and a thinner cloud; as the temperature inversion strengthens this response also increases. The 1000 m setup represents an extreme case of this scenario, whereas in the 800 m setup the enhanced coupling is sufficient to produce an increase in sub-cloud moisture flux during the afternoon, which acts to partially mitigate the cloud thinning.

4 Discussion and conclusions

Figure 11 summarizes the findings of this study. The SDE manifests itself as a modification to the processes that maintain the supply of moisture to the cloud layer and are ultimately driven by the strengthened inversion layer and weakened entrainment rate caused by an absorbing aerosol layer above the inversion. The initial sequence of responses to an elevated layer of absorbing aerosol is summarized below, with numbers referring to each response labelled in Fig. 11.

1. The absorbing aerosol layer produces a heat perturbation that results in a strengthened temperature inversion.

2. Buoyant parcels of air in the BL require more energy in order to push through the strengthened temperature inversion. This weakens the entrainment rate (w_e) across the inversion layer.

3a. Weakened entrainment results in a decrease in the cloud-top altitude and BL depth.

3b. The reduction in the entrainment of warm and dry air from the FT reduces the amount of mixing, reducing the sink of q_t in the cloud layer and allowing the BL to maintain a greater RH. The result is an increase in $\overline{q_t}$, a small decrease in BL temperature, and an increase in RH.

3c. Weakened entrainment reduces the production of buoyancy from the evaporative cooling of entrained air, causing a decrease in BL dynamics ($\overline{w'w'}$), especially overnight.

4a. Cloud-top longwave cooling remains largely unchanged due to the weak sensitivity to LWPs larger than $50\,\mathrm{g\,m^{-2}}$ overnight and the relatively small changes in LWP during the daytime. The insulating effect of the aerosol layer only weakly influences the net longwave fluxes and divergence above the cloud.

4b. Increased $\overline{q_t}$ in the BL and weakened BL dynamics reduce the evaporation rate of water from the surface, as evidenced by the reduction in latent heat flux (LHF).

According to the model sensitivity simulations presented, SDE is amplified through the following mechanisms:

- geometrically thinner aerosol layers of high aerosol density and low SSA, which produce a stronger localized heat perturbation;
- aerosol layers close to the inversion, while larger cloud–aerosol gaps result in a delayed and weaker cloud response; and
- warmer SSTs, which enhance the flux of moisture to the BL. As a secondary response, the increased SST also drives a stronger reduction in LHF and causes the BL to adjust at a quicker rate.

Conversely, SDE is reduced by the following:

- precipitation that, as a sink of cloud liquid water, dampens the cloud response (it follows that any feedbacks that result in an increase in precipitation further weakens the SDE);
- increases in the large-scale advective heat tendency (stronger cooling), which are balanced by enhanced buoyancy production from w_e and a more rapid BL adjustment; and
- an increase in the moisture content of the FT, which increases the role that entrainment plays in the supply of moisture to the BL.

Finally, an increase in the degree of decoupling in the BL increases the sensitivity of the BL dynamics to changes in w_e, driving towards a positive daily mean SDE. Extreme cases result in a strong positive SDE from day 2 after applying the aerosol perturbation.

Several feedbacks between responses occur as the BL adjusts to the perturbations. The key feedbacks occur in the sub-cloud layer and can work together to greatly reduce the supply of moisture to the cloud layer. Processes that act to decrease $\overline{w'w'}$ also further decrease w_e and the LHF; these changes weaken the response of $\overline{q_t}$ in the BL so that there is a weaker flux of q_v to the cloud layer. Reduced w_e and a reduction in condensation at the base of the cloud layer weaken buoyancy production in the cloud layer, which acts to further decrease $\overline{w'w'}$ and w_e. These feedbacks are most pronounced during the cloud growth phase overnight when the diurnal cycles of w_e, $\overline{w'w'}$, and LHF peak, resulting in a weakened cloud growth phase and a thinner cloud overnight and into the morning when the aerosol layer is present, thus producing a positive SDE. Longwave cloud-top cooling is only weakly sensitive to changes in LWP above $50\,\mathrm{g\,m^{-2}}$, and therefore we do not see changes in the buoyancy production from this process unless the LWP is significantly impacted, which occurs when the BL is decoupled. In this case the reduced LWP further weakens the buoyancy production in the cloud layer and consequently w_e and BL dynamics.

A second adjustment feedback on the cloud maintenance occurs through the reduced depth of the BL, which acts to promote coupling of the cloud and sub-cloud layers. In this case the feedback mechanism outlined previously acts in reverse so that $\overline{w'w'}$, LHF, and the supply of q_v to the cloud layer increase. This weaker feedback mechanism likely occurs throughout the diurnal cycle but only becomes important at midday when BL dynamics and sub-cloud moisture fluxes are at their weakest and most sensitive to small changes. This adjustment results in reduced cloud decay throughout the afternoon and a thicker cloud, and thus negative SDE, when the elevated layer of absorbing aerosol is present. The strength of this feedback mechanism decreases as the degree of BL decoupling increases until the mechanism ceases to have any impact on the BL; in our study this occurs when the BL is 1000 m deep.

The sign and magnitude of the SDE from elevated layers of absorbing aerosol are sensitive to the layer properties and BL properties, especially the diurnal variations in coupling between the cloud and sub-cloud layers. For coupled BLs, the SDE on the first day after adding the absorbing aerosol layer is slightly positive unless the aerosol layer is close to the inversion layer. On the second and third day the SDE is strongly negative and peaks on the second day. Generally, for coupled BLs the SDE is of opposite sign to the DRE and

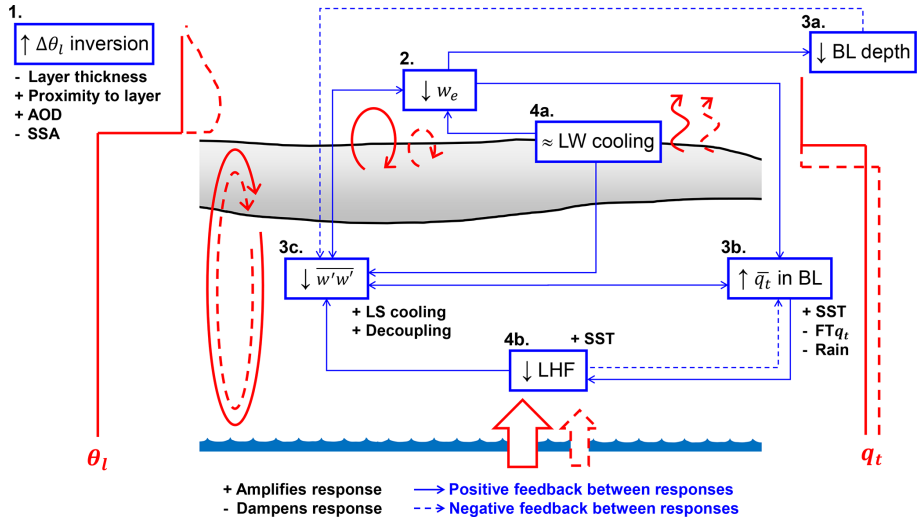

Figure 11. Summary of how the semi-direct effect manifests in a cross section of a stratocumulus-topped boundary layer. Solid red lines refer to the no-aerosol simulation and dashed red lines to the elevated absorbing aerosol layer simulations. Key responses to the boundary layer profiles are depicted in the blue boxes and include the strength of the inversion layer ($\Delta\theta_l$ inversion), entrainment rate (w_e), boundary layer depth (BL depth), cloud-top longwave cooling (LW cooling), mean vertical motions in the boundary layer ($\overline{w'w'}$), mean total water content of the BL ($\overline{q_t}$), and the latent heat flux at the ocean surface (LHF). Solid (dashed) arrows between boxes represent positive (negative) feedbacks between responses. For each response we include properties of the aerosol layer, boundary layer, or model setup that amplify (denoted by $+$) or dampen (denoted by $-$) the response; this includes the aerosol layer thickness (Layer thickness), cloud–aerosol gap (Proximity to layer), the aerosol optical depth of the layer (AOD), the single-scattering albedo of the aerosol layer (SSA), the sea surface temperature (SST), the water content of the free troposphere (FTq_t), precipitation (Rain), large-scale advective heat tendency (LS cooling), and the degree of boundary layer decoupling (Decoupling).

often greater in magnitude, resulting in a small or negative total radiative effect for aerosol–radiation interactions from elevated absorbing aerosol layers. For BLs that show characteristics of being decoupled for most of the diurnal cycle the SDE is positive for all 3 d and increases in magnitude throughout; as the BL becomes more decoupled the magnitude of the SDE increases. For decoupled BLs the SDE acts to enhance the DRE, resulting in a larger total radiative effect.

The increased LWP and negative SDE in the well-mixed coupled BL experiments are consistent with satellite observations over the southeast Atlantic from Adebiyi and Zuidema (2018) and Wilcox (2012). However, our LEM simulations suggest a positive SDE in decoupled BL regions, such as near the stratocumulus-to-cumulus transition region. In reality, the BL may not be as decoupled as in the simulations. The deepening BL is usually accompanied by an increasing SST (Sandu and Stevens, 2011), which was not represented in our simulations; the increase in SST would provide a considerably larger flux of moisture from the surface and enhance the production of buoyancy at the surface, which may act to weaken the sensitivity of the BL to changes in dynamics. The aerosol layer sensitivity experiments in Sect. 3.3 suggest that the daily mean SDE strongly weakens as the distance of the gap between the cloud top and aerosol layer increases. Table 3 shows that on the second day of the simulation no gap results in a daily mean SDE of $-7\,\mathrm{W\,m^{-2}}$ compared to $-0.4\,\mathrm{W\,m^{-2}}$ for a 500 m gap. Additionally, even for a large perturbation (AOD of 0.5) the daily mean SDE in the initial 24 h of the 50 m gap experiment is only $1\,\mathrm{W\,m^{-2}}$. These results are in general agreement with the stratocumulus-to-cumulus transition LES studies by Yamaguchi et al. (2015) and Zhou et al. (2017), which suggest that only those elevated smoke layers that are very close to, or in direct contact with, the cloud layer impact the cloud properties. Combined with the satellite observations in Fig. 1 these results suggest that the overall SDE from elevated layers of aerosol over the southeast Atlantic is weak. However, it is worth noting that Yamaguchi et al. (2015) and Zhou et al. (2017) used the same case study (Sandu and Stevens, 2011) yet found opposing results on whether the absorbing aerosol layer inhibits or hastens the transition to cumulus. Yamaguchi et al. (2015) state that throughout their simulations the BL is decoupled below 800 m, whereas in Zhou et al. (2017) vertical mixing within the BL continues until the inversion height exceeds ~ 1.4 km (Zhou et al., 2017; Fig. 1b). Our results highlight the fact that the cloud response is sensitive to the diurnal variations in BL mixing, which may explain these opposing results. Additionally, inconsistent responses between LES models can also arise through differences in the representation of processes, including unresolved sub-grid-scale turbulence (Stevens et al., 2005) and

microphysics (van der Dussen et al., 2013). Our results show that the heat perturbation above the cloud layer impacts all aspects of the BL profile; therefore, it would be beneficial to repeat this study using other LES models to test our conclusions.

Satellite products provide an excellent opportunity to observe aerosol–cloud and aerosol–radiation interactions in remote locations such as the southeast Atlantic Ocean; however, most instruments are on polar-orbiting satellites that only provide observations from a limited window within the diurnal cycle of the clouds. Our simulations suggest that the cloud response to elevated absorbing aerosol layers and the SDE display important diurnal variations, so a single observation is unlikely to be representative of the daily mean response. Important changes to the cloud properties occur overnight and play a considerable role in the SDE of the morning period, yet little is known about the impact from absorbing aerosol layers overnight. Future studies should use geostationary satellite observations to investigate the full diurnal cycle of the SDE.

For a well-mixed coupled BL, the initial cloud and radiative responses depend on small-scale processes, such as entrainment and turbulence, which must be parameterized in climate models. Gordon et al. (2018) used a nested regional model within the Hadley Centre Global Environment Model (HadGEM) to investigate the impact of an incoming elevated plume of smoke in the southeast Atlantic. They found that the elevated aerosol layer reduced cloud-top height and enhanced LWP through a reduction in w_e driven by localized heating at or just above the cloud layer of ~ 6 K. The importance of the weakened w_e aligns well with the LES results of the present study, but the magnitudes of the cloud and radiative response are much greater in HadGEM, with an LWP increase of 90 %, an increase in cloud fraction of 19 %, and a mean SDE of $-30\,\mathrm{W\,m^{-2}}$. Gordon et al. (2018) do not find a consistent longer-term (~ 3 d) reduction in LWP following BL adjustments. In the simulations presented here, the cloud fraction remained ~ 100 %, which may explain the smaller SDE than that found by Gordon et al. (2018). Additionally, concurrent aerosol-cloud interactions may modify the underlying cloud properties, which may act to amplify the SDE. The lack of BL adjustment may be due to processes that are not explicitly treated in HadGEM, such as BL turbulence and subsequent missing feedbacks on surface fluxes, or due to aerosol–cloud interactions not represented in the LES. Alternatively, differences may be due to different simulated cases. The trajectory analysis of Gordon et al. (2018) suggests that their BL air mass traverses the study region more quickly than the absorbing aerosol layer, which may prevent the BL adjustments from occurring.

In our simulations the SST and subsidence rate are held constant for the whole duration, whereas real stratocumulus decks tend to experience an increasing SST and decreasing subsidence rate. An increasing SST increases surface latent heat fluxes, cloud liquid water content, and the strength of BL eddies; it also acts to deepen the BL through increased entrainment and enhance decoupling of the sub-cloud layer (Bretherton and Wyant, 1997). As the cloud is advected over the warmer sea surface, the enhanced flux of moisture would act to increase the magnitude of the SDE and prevent the BL from drying out as quickly. Simultaneously, the enhanced decoupling of the sub-cloud layer may result in BL dynamical feedbacks that result in a reduction in LWP (see Fig. 10). Our model uses an Eulerian framework whereby the absorbing aerosol layer remains at a constant height above the cloud, whereas the heat perturbation is allowed to subside into the cloud. In reality the aerosol layer may also subside. The sensitivity experiments in Sect. 3.3 show that as the aerosol layer approaches the cloud layer, the SDE increases; therefore, if we were to represent aerosol layer subsidence we would expect an enhanced cloud response and SDE.

Changes to the aerosol distribution within the cloud or in the cloud droplet distribution have not been considered in this study. A weakened w_e increases condensate in the cloud and likely results in an increase in cloud droplet effective radius (r_e). This would promote warm rain processes and enhance precipitation, thus reducing the LWP and amplifying the reduction in BL dynamics. These combined effects could lead to a decrease in LWP and shift the SDE towards a positive sign at a quicker rate than suggested by the LES. For the cases in which the aerosol layer is directly above the cloud layer an enhanced flux of CCN into the BL would be expected and would act to reduce r_e, suppress precipitation, and act to enhance buoyancy production. However, in situ observations routinely find that the layers of smoke over the southeast Atlantic are embedded in moist layers (Adebiyi et al., 2015), which could increase the flux of water from the free troposphere and act to mitigate the changes that occur alongside an increased CCN. The introduction of the absorbing aerosol into the cloud layer would additionally enhance cloud evaporation and act to thin the cloud layer (Hill and Dobbie, 2008; Johnson et al., 2004). Thus, although the experiments in which the aerosol layer is directly above the inversion result in the most strongly negative SDE, the response would be at least partially mitigated if the aerosol distribution was represented explicitly, further decreasing the role that SDE plays in the total radiative effect of elevated layers of absorbing aerosol. Extending the present study using a binned microphysics scheme would include the additional response of the droplet size distribution, and using an aerosol scheme would include the additional impacts the weakened w_e has on the availability of CCN and subsequent cloud response.

Appendix A

This Appendix describes how the AOD and SSA are prescribed in elevated aerosol layer experiments, along with the geometric thickness of the aerosol layer and the distance between the inversion layer and the aerosol base. In each call to the radiation scheme the desired AOD and SSA are used to determine the mass mixing ratio of two aerosol species: water-soluble like (WS) and biomass burning like (BB).

For a single wavelength, the AOD between the altitudes z_0 and z, corresponding to the base and top of the aerosol layer, respectively, is calculated as

$$\mathrm{AOD} = \sum_{i=z_0}^{z} \sum_{j=\mathrm{WS,BB}} \left(K_{\mathrm{scat}_j} + K_{\mathrm{abs}_j}\right) \cdot q_{i,j} \cdot \rho_i \cdot \mathrm{d}z_i, \quad \text{(A1)}$$

where K_{scat} and K_{abs} are the specific scattering and absorption coefficients, respectively, for the aerosol species j ($\mathrm{m^2\,kg^{-1}}$), with a mass mixing ratio q ($\mathrm{kg\,kg^{-1}_{dry}}$) at each model level i of geometric thickness $\mathrm{d}z$ (in metres) and density of dry air ρ ($\mathrm{kg\,m^{-3}}$). If the mass mixing ratio of each species is assumed equal and constant with height ($q_{\mathrm{WS}} = q_{\mathrm{BB}}$ and $q_i = q$), Eq. (A1) becomes

$$q \cdot \sum_{i=z_0}^{z} \rho_i \cdot \mathrm{d}z_i = \frac{\mathrm{AOD}}{\sum\limits_{j=\mathrm{WS,BB}} K_{\mathrm{scat}_j} + K_{\mathrm{abs}_j}}. \quad \text{(A2)}$$

We incorporate a factor X_{SSA} into Eq. (A2) that can be used to describe the relative ratio of WS mass to BB mass so that Eq. (A2) becomes

$$q \cdot \sum_{i=z_0}^{z} \rho_i \cdot \mathrm{d}z_i = \frac{\mathrm{AOD}}{\left(K_{\mathrm{scat_{WS}}} + K_{\mathrm{abs_{WS}}}\right) + X_{\mathrm{SSA}} \cdot \left(K_{\mathrm{scat_{BB}}} + K_{\mathrm{abs_{BB}}}\right)}. \quad \text{(A3)}$$

Equation (A3) can be rearranged to give q for a given AOD:

$$q = \frac{\mathrm{AOD_{constant}}}{\sum\limits_{i=z_0}^{z} \rho_i \cdot \mathrm{d}z_i}, \quad \text{(A4)}$$

where

$$\mathrm{AOD_{constant}} = \frac{\mathrm{AOD}}{\left(K_{\mathrm{scat_{WS}}} + K_{\mathrm{abs_{WS}}}\right) + X_{\mathrm{SSA}} \cdot \left(K_{\mathrm{scat_{BB}}} + K_{\mathrm{abs_{BB}}}\right)}. \quad \text{(A5)}$$

Therefore, for the two aerosol species

$$q_j = \begin{cases} q, & j = \mathrm{WS} \\ X_{\mathrm{SSA}} \cdot q, & j = \mathrm{BB}. \end{cases} \quad \text{(A6)}$$

The overall SSA is calculated as

$$\mathrm{SSA} = \frac{K_{\mathrm{scatWS}} + X_{\mathrm{SSA}} \cdot K_{\mathrm{scatBB}}}{K_{\mathrm{scatWS}} + X_{\mathrm{SSA}} \cdot K_{\mathrm{scatBB}} + K_{\mathrm{absWS}} + X_{\mathrm{SSA}} \cdot K_{\mathrm{absBB}}}. \quad \text{(A7)}$$

Equation (A7) can be rearranged to solve for X_{SSA} as

$$X_{\mathrm{SSA}} = \frac{K_{\mathrm{scat_{WS}}} - \mathrm{SSA} \cdot \left(K_{\mathrm{scat_{WS}}} + K_{\mathrm{abs_{WS}}}\right)}{\mathrm{SSA} \cdot \left(K_{\mathrm{scat_{BB}}} + K_{\mathrm{abs_{BB}}}\right) - K_{\mathrm{scat_{BB}}}}. \quad \text{(A8)}$$

At the beginning of the simulation X_{SSA} and $\mathrm{AOD_{constant}}$ are calculated using Eqs. (A8) and (A5), respectively, using the shortwave extinction coefficients of the aerosols for the wavelength band 320–690 nm and the prescribed AOD and SSA. At each horizontal grid point q is then calculated using Eq. (A4) for the elevated aerosol layer, where z_0 is the base of the aerosol layer, and z is the top of the aerosol layer. The mass mixing ratio of each species is calculated using Eq. (A6), and finally the mass mixing ratio profiles of WS and BB are applied to the radiation scheme.

Data availability. Data and relevant information for reproducing Figs. 3–11 have been uploaded to Zenodo and can be accessed via: https://doi.org/10.5281/zenodo.3630557 (Herbert et al., 2020).

Supplement. The supplement related to this article is available online at: https://doi.org/10.5194/acp-20-1317-2020-supplement.

Author contributions. RJH, NB, EJH, and AAH designed the methodology and experiments. AAH provided model expertise and assistance. RJH set up, performed, and post-processed the simulations. RJH, NB, EJH, and AAH analysed the results. RJH provided all visualizations and wrote the initial paper draft. NB, EJH, and AAH provided revisions and commentary on the paper.

Competing interests. The authors declare that they have no conflict of interest.

Special issue statement. This article is part of the special issue "New observations and related modelling studies of the aerosol–cloud–climate system in the Southeast Atlantic and southern Africa regions (ACP/AMT inter-journal SI)". It is not associated with a conference.

Acknowledgements. This research was funded by the UK Natural Environment Research Council (NERC) CLouds and Aerosol Radiative Impacts and Forcing: Year 2016 (CLARIFY-2016) project NE/L013479/1. We acknowledge use of the Monsoon system, a collaborative facility supplied under the Joint Weather and Climate Research Programme, a strategic partnership between the Met Office and the Natural Environment Research Council. The CALIOP data were obtained from the NASA Langley Research Center Atmospheric Science Data Center https://eosweb.larc.nasa.gov/project/calipso/calipso_table (last access: 1 August 2017). The CATS data were obtained from NASA Goddard Space Flight Center https://cats.gsfc.nasa.gov (last access: 31 July 2019).

Financial support. This research has been supported by NERC (grant no. NE/L013479/1).

Review statement. This paper was edited by Jérôme Riedi and reviewed by three anonymous referees.

References

Abel, S. J., Walters, D. N., and Allen, G.: Evaluation of stratocumulus cloud prediction in the Met Office forecast model during VOCALS-REx, Atmos. Chem. Phys., 10, 10541–10559, https://doi.org/10.5194/acp-10-10541-2010, 2010.

Ackerman, A. S., vanZanten, M. C., Stevens, B., Savic-Jovcic, V., Bretherton, C. S., Chlond, A., Golaz, J.-C., Jiang, H., Khairoutdinov, M., Krueger, S. K., Lewellen, D. C., Lock, A., Moeng, C.-H., Nakamura, K., Petters, M. D., Snider, J. R., Weinbrecht, S., and Zulauf, M.: Large-Eddy Simulations of a Drizzling, Stratocumulus-Topped Marine Boundary Layer, Mon. Weather Rev., 137, 1083–1110, https://doi.org/10.1175/2008MWR2582.1, 2009.

Adebiyi, A. A. and Zuidema, P.: Low cloud cover sensitivity to biomass-burning aerosols and meteorology over the Southeast Atlantic, J. Climate, 31, 4329–4346, https://doi.org/10.1175/JCLI-D-17-0406.1, 2018.

Adebiyi, A. A., Zuidema, P., and Abel, S. J.: The convolution of dynamics and moisture with the presence of shortwave absorbing aerosols over the southeast Atlantic, J. Climate, 28, 1997–2024, https://doi.org/10.1175/JCLI-D-14-00352.1, 2015.

Albrecht, B. A., Jensen, M. P., and Syrett, W. J.: Marine boundary layer structure and fractional cloudiness, J. Geophys. Res., 100, 14209–14222, https://doi.org/10.1029/95JD00827, 1995.

Bond, T. C., Doherty, S. J., Fahey, D. W., Forster, P. M., Berntsen, T., DeAngelo, B. J., Flanner, M. G., Ghan, S., Kärcher, B., Koch, D., Kinne, S., Kondo, Y., Quinn, P. K., Sarofim, M. C., Schultz, M. G., Schulz, M., Venkataraman, C., Zhang, H., Zhang, S., Bellouin, N., Guttikunda, S. K., Hopke, P. K., Jacobson, M. Z., Kaiser, J. W., Klimont, Z., Lohmann, U., Schwarz, J. P., Shindell, D., Storelvmo, T., Warren, S. G., and Zender, C. S.: Bounding the role of black carbon in the climate system: A scientific assessment, J. Geophys. Res.-Atmos., 118, 5380–5552, https://doi.org/10.1002/jgrd.50171, 2013.

Bony, S. and Dufresne, J. L.: Marine boundary layer clouds at the heart of tropical cloud feedback uncertainties in climate models, Geophys. Res. Lett., 32, 1–4, https://doi.org/10.1029/2005GL023851, 2005.

Boucher, O., Randall, D., Artaxo, P., Bretherton, C., Feingold, G., Forster, P., Kerminen, V.-M., Kondo, Y., Liao, H., Lohmann, U., Rasch, P., Satheesh, S. K., Sherwood, S., Stevens, B., and Zhang, X.-Y.: IPCC AR5 Clouds and Aerosols, in: Climate Change 2013 – The Physical Science Basis, 571–658, Cambridge University Press, Cambridge, UK and New York, NY, USA, 2013.

Bretherton, C. S. and Wyant, M. C.: Moisture Transport, Lower-Tropospheric Stability, and Decoupling of Cloud-Topped Boundary Layers, J. Atmos. Sci., 54, 148–167, https://doi.org/10.1175/1520-0469(1997)054<0148:MTLTSA>2.0.CO;2, 1997.

Bretherton, C. S., Blossey, P. N., and Jones, C. R.: Mechanisms of marine low cloud sensitivity to idealized climate perturbations: A single-LES exploration extending the CGILS cases, J. Adv. Model. Earth Sy., 5, 316–337, https://doi.org/10.1002/jame.20019, 2013.

Chand, D., Wood, R., Anderson, T. L., Satheesh, S. K., and Charlson, R. J.: Satellite-derived direct radiative effect of aerosols dependent on cloud cover, Nat. Geosci., 2, 181–184, https://doi.org/10.1038/ngeo437, 2009.

Costantino, L. and Bréon, F.-M.: Aerosol indirect effect on warm clouds over South-East Atlantic, from co-located MODIS and CALIPSO observations, Atmos. Chem. Phys., 13, 69–88, https://doi.org/10.5194/acp-13-69-2013, 2013.

Das, S., Harshvardhan, H., Bian, H., Chin, M., Curci, G., Protonotariou, A. P., Mielonen, T., Zhang, K., Wang, H., and Liu, X.: Biomass burning aerosol transport and vertical distribution over

the South African-Atlantic region, J. Geophys. Res., 122, 6391–6415, https://doi.org/10.1002/2016JD026421, 2017.

De Roode, S. R., Siebesma, A. P., Gesso, S. D., Jonker, H. J. J., Schalkwijk, J., and Sival, J.: A mixed-layer model study of the stratocumulus response to changes in large-scale conditions, J. Adv. Model. Earth Sy., 6, 1256–1270, https://doi.org/10.1002/2014MS000347, 2014.

de Roode, S. R., Sandu, I., van der Dussen, J. J., Ackerman, A. S., Blossey, P., Jarecka, D., Lock, A., Siebesma, A. P., and Stevens, B.: Large-Eddy Simulations of EUCLIPSE–GASS Lagrangian Stratocumulus-to-Cumulus Transitions: Mean State, Turbulence, and Decoupling, J. Atmos. Sci., 73, 2485–2508, https://doi.org/10.1175/JAS-D-15-0215.1, 2016.

Edwards, J. M. and Slingo, A.: Studies with a flexible new radiation code. I: Choosing a configuration for a large-scale model, Q. J. Roy. Meteor. Soc., 122, 689–719, https://doi.org/10.1256/smsqj.53106, 1996.

Efstathiou, G. A. and Beare, R. J.: Quantifying and improving sub-grid diffusion in the boundary-layer grey zone, Q. J. Roy. Meteor. Soc., 141, 3006–3017, https://doi.org/10.1002/qj.2585, 2015.

Efstathiou, G. A., Beare, R. J., Osborne, S., and Lock, A. P.: Grey zone simulations of the morning convective boundary layer development, J. Geophys. Res.-Atmos., 121, 4769–4782, https://doi.org/10.1002/2016JD024860, 2016.

Feingold, G., Koren, I., Wang, H., Xue, H., and Brewer, W. A.: Precipitation-generated oscillations in open cellular cloud fields, Nature, 466, 849–852, https://doi.org/10.1038/nature09314, 2010.

Garrett, T. J. and Zhao, C.: Increased Arctic cloud longwave emissivity associated with pollution from mid-latitudes, Nature, 440, 787–789, https://doi.org/10.1038/nature04636, 2006.

Gordon, H., Field, P. R., Abel, S. J., Dalvi, M., Grosvenor, D. P., Hill, A. A., Johnson, B. T., Miltenberger, A. K., Yoshioka, M., and Carslaw, K. S.: Large simulated radiative effects of smoke in the south-east Atlantic, Atmos. Chem. Phys., 18, 15261–15289, https://doi.org/10.5194/acp-18-15261-2018, 2018.

Gray, M. E. B., Brown, A. R., Lock, A. P., and Petch, J.: Version 2.3 Of The Met Office Large Eddy Model: Part III. Software Documentation, Met Office, Bracknell, UK, 2001.

Hartmann, D. L. and Short, D. A.: On the Use of Earth Radiation Budget Statistics for Studies of Clouds and Climate, J. Atmos. Sci., 37, 1233–1250, https://doi.org/10.1175/1520-0469(1980)037<1233:OTUOER>2.0.CO;2, 1980.

Hartmann, D. L., Ockert-Bell, M. E., and Michelsen, M. L.: Hartmann_EtAl_1992_EnergyBalance, J. Climate, 5, 1281–1304, https://doi.org/10.1175/1520-0442(1992)005<1281:Teocto>2.0.Co;2, 1992.

Herbert, R., Bellouin, N., Highwood, E., and Hill, A.: Diurnal cycle of the semi-direct effect from a persistent absorbing aerosol layer over marine stratocumulus in large-eddy simulations: supporting dataset, Zenodo, https://doi.org/10.5281/zenodo.3630557, 2020.

Hignett, P.: Observations of Diurnal Variation in a Cloud-capped Marine Boundary Layer, J. Atmos. Sci., 48, 1474–1482, https://doi.org/10.1175/1520-0469(1991)048<1474:OODVIA>2.0.CO;2, 1991.

Hill, A. A. and Dobbie, S.: The impact of aerosols on non-precipitating marine stratocumulus. II: The semi-direct effect, Q. J. Roy. Meteor. Soc., 134, 1155–1165, https://doi.org/10.1002/qj.277, 2008.

Hill, A. A., Dobbie, S., and Yin, Y.: The impact of aerosols on non-precipitating marine stratocumulus. I: Model description and prediction of the indirect effect, Q. J. Roy. Meteor. Soc., 134, 1143–1154, https://doi.org/10.1002/qj.278, 2008.

Hill, A. A., Feingold, G., and Jiang, H.: The Influence of Entrainment and Mixing Assumption on Aerosol–Cloud Interactions in Marine Stratocumulus, J. Atmos. Sci., 66, 1450–1464, https://doi.org/10.1175/2008JAS2909.1, 2009.

Hill, A. A., Field, P. R., Furtado, K., Korolev, A., and Shipway, B. J.: Mixed-phase clouds in a turbulent environment. Part 1: Large-eddy simulation experiments, Q. J. Roy. Meteor. Soc., 140, 855–869, https://doi.org/10.1002/qj.2177, 2014.

Johnson, B. T., Shine, K. P., and Forster, P. M.: The semi-direct aerosol effect: Impact of absorbing aerosols on marine stratocumulus, Q. J. Roy. Meteor. Soc., 130, 1407–1422, https://doi.org/10.1256/qj.03.61, 2004.

Kato, S., Sun-Mack, S., Miller, W. F., Rose, F. G., Chen, Y., Minnis, P., and Wielicki, B. A.: Relationships among cloud occurrence frequency, overlap, and effective thickness derived from CALIPSO and CloudSat merged cloud vertical profiles, J. Geophys. Res., 115, D00H28, https://doi.org/10.1029/2009JD012277, 2010.

Kato, S., Rose, F. G., Sun-Mack, S., Miller, W. F., Chen, Y., Rutan, D. A., Stephens, G. L., Loeb, N. G., Minnis, P., Wielicki, B. A., Winker, D. M., Charlock, T. P., Stackhouse, P. W., Xu, K.-M., and Collins, W. D.: Improvements of top-of-atmosphere and surface irradiance computations with CALIPSO-, CloudSat-, and MODIS-derived cloud and aerosol properties, J. Geophys. Res., 116, D19209, https://doi.org/10.1029/2011JD016050, 2011.

Klein, S. A., Hall, A., Norris, J. R., and Pincus, R.: Low-Cloud Feedbacks from Cloud-Controlling Factors: A Review, Surv. Geophys., 38, 1307–1329, https://doi.org/10.1007/s10712-017-9433-3, 2017.

Koch, D. and Del Genio, A. D.: Black carbon semi-direct effects on cloud cover: review and synthesis, Atmos. Chem. Phys., 10, 7685–7696, https://doi.org/10.5194/acp-10-7685-2010, 2010.

Lee, I. Y.: Evaluation of cloud microphysics parameterizations for mesoscale simulations, Atmos. Res., 24, 209–220, https://doi.org/10.1016/0169-8095(89)90046-X, 1989.

Leon, D. C., Wang, Z., and Liu, D.: Climatology of drizzle in marine boundary layer clouds based on 1 year of data from CloudSat and Cloud-Aerosol Lidar and Infrared Pathfinder Satellite Observations (CALIPSO), J. Geophys. Res.-Atmos., 114, D00A14, https://doi.org/10.1029/2008JD009835, 2009.

Lu, Z., Liu, X., Zhang, Z., Zhao, C., Meyer, K., Rajapakshe, C., Wu, C., Yang, Z., and Penner, J. E.: Biomass smoke from southern Africa can significantly enhance the brightness of stratocumulus over the southeastern Atlantic Ocean, P. Natl. Acad. Sci. USA, 115, 2924–2929, https://doi.org/10.1073/pnas.1713703115, 2018.

Monin, A. S. and Obukhov, A. M.: Basic laws of turbulent mixing in the surface layer of the atmosphere, Geophys. Dir. AF Cambridge Res. Cent., 24, 163–187, https://doi.org/10.1016/j.jallcom.2004.05.088, 1954.

Muhlbauer, A., McCoy, I. L., and Wood, R.: Climatology of stratocumulus cloud morphologies: microphysical properties and radiative effects, Atmos. Chem. Phys., 14, 6695–6716, https://doi.org/10.5194/acp-14-6695-2014, 2014.

Ovchinnikov, M., Ackerman, A. S., Avramov, A., Cheng, A., Fan, J., Fridlind, A. M., Ghan, S., Harrington, J., Hoose, C., Korolev, A., McFarquhar, G. M., Morrison, H., Paukert, M., Savre, J., Shipway, B. J., Shupe, M. D., Solomon, A., and Sulia, K.: Intercomparison of large-eddy simulations of Arctic mixed-phase clouds: Importance of ice size distribution assumptions, J. Adv. Model. Earth Sy., 6, 223–248, https://doi.org/10.1002/2013MS000282, 2014.

Painemal, D., Kato, S., and Minnis, P.: Boundary layer regulation in the southeast Atlantic cloud microphysics during the biomass burning season as seen by the A-train satellite constellation, J. Geophys. Res., 119, 11288–11302, https://doi.org/10.1002/2014JD022182, 2014.

Peers, F., Bellouin, N., Waquet, F., Ducos, F., Goloub, P., Mollard, J., Myhre, G., Skeie, R. B., Takemura, T., Tanré, D., Thieuleux, F., and Zhang, K.: Comparison of aerosol optical properties above clouds between POLDER and AeroCom models over the South East Atlantic Ocean during the fire season, Geophys. Res. Lett., 43, 3991–4000, https://doi.org/10.1002/2016GL068222, 2016.

Penner, J. E., Zhang, S. Y., and Chuang, C. C.: Soot and smoke aerosol may not warm climate, J. Geophys. Res.-Atmos., 108, https://doi.org/10.1029/2003JD003409, 2003.

Rajapakshe, C., Zhang, Z., Yorks, J. E., Yu, H., Tan, Q., Meyer, K., Platnick, S., and Winker, D. M.: Seasonally transported aerosol layers over southeast Atlantic are closer to underlying clouds than previously reported, Geophys. Res. Lett., 44, 5818–5825, https://doi.org/10.1002/2017GL073559, 2017.

Sakaeda, N., Wood, R., and Rasch, P. J.: Direct and semidirect aerosol effects of southern African biomass burning aerosol, J. Geophys. Res., 116, D12205, https://doi.org/10.1029/2010JD015540, 2011.

Sandu, I. and Stevens, B.: On the Factors Modulating the Stratocumulus to Cumulus Transitions, J. Atmos. Sci., 68, 1865–1881, https://doi.org/10.1175/2011JAS3614.1, 2011.

Sandu, I., Stevens, B., and Pincus, R.: On the transitions in marine boundary layer cloudiness, Atmos. Chem. Phys., 10, 2377–2391, https://doi.org/10.5194/acp-10-2377-2010, 2010.

Sherwood, S. C., Bony, S., Boucher, O., Bretherton, C., Forster, P. M., Gregory, J. M., Stevens, B., Sherwood, S. C., Bony, S., Boucher, O., Bretherton, C., Forster, P. M., Gregory, J. M., and Stevens, B.: Adjustments in the Forcing-Feedback Framework for Understanding Climate Change, B. Am. Meteorol. Soc., 96, 217–228, https://doi.org/10.1175/BAMS-D-13-00167.1, 2015.

Stevens, B., Moeng, C.-H., Ackerman, A. S., Bretherton, C. S., Chlond, A., de Roode, S., Edwards, J., Golaz, J.-C., Jiang, H., Khairoutdinov, M., Kirkpatrick, M. P., Lewellen, D. C., Lock, A., Müller, F., Stevens, D. E., Whelan, E., and Zhu, P.: Evaluation of Large-Eddy Simulations via Observations of Nocturnal Marine Stratocumulus, Mon. Weather Rev., 133, 1443–1462, https://doi.org/10.1175/MWR2930.1, 2005.

Stjern, C. W., Samset, B. H., Myhre, G., Forster, P. M., Hodnebrog, Ø., Andrews, T., Boucher, O., Faluvegi, G., Iversen, T., Kasoar, M., Kharin, V., Kirkevåg, A., Lamarque, J. F., Olivié, D., Richardson, T., Shawki, D., Shindell, D., Smith, C. J., Takemura, T., and Voulgarakis, A.: Rapid Adjustments Cause Weak Surface Temperature Response to Increased Black Carbon Concentrations, J. Geophys. Res.-Atmos., 122, 11462–11481, https://doi.org/10.1002/2017JD027326, 2017.

van der Dussen, J. J., de Roode, S. R., Ackerman, A. S., Blossey, P. N., Bretherton, C. S., Kurowski, M. J., Lock, A. P., Neggers, R. A. J., Sandu, I., and Siebesma, A. P.: The GASS/EUCLIPSE model intercomparison of the stratocumulus transition as observed during ASTEX: LES results, J. Adv. Model. Earth Syst., 5, 483–499, https://doi.org/10.1002/jame.20033, 2013.

Wilcox, E. M.: Stratocumulus cloud thickening beneath layers of absorbing smoke aerosol, Atmos. Chem. Phys., 10, 11769–11777, https://doi.org/10.5194/acp-10-11769-2010, 2010.

Wilcox, E. M.: Direct and semi-direct radiative forcing of smoke aerosols over clouds, Atmos. Chem. Phys., 12, 139–149, https://doi.org/10.5194/acp-12-139-2012, 2012.

Wood, R.: Stratocumulus Clouds, Mon. Weather Rev., 140, 2373–2423, https://doi.org/10.1175/MWR-D-11-00121.1, 2012.

Wyant, M. C., Wood, R., Bretherton, C. S., Mechoso, C. R., Bacmeister, J., Balmaseda, M. A., Barrett, B., Codron, F., Earnshaw, P., Fast, J., Hannay, C., Kaiser, J. W., Kitagawa, H., Klein, S. A., Köhler, M., Manganello, J., Pan, H.-L., Sun, F., Wang, S., and Wang, Y.: The PreVOCA experiment: modeling the lower troposphere in the Southeast Pacific, Atmos. Chem. Phys., 10, 4757–4774, https://doi.org/10.5194/acp-10-4757-2010, 2010.

Yamaguchi, T., Feingold, G., Kazil, J., and McComiskey, A.: Stratocumulus to cumulus transition in the presence of elevated smoke layers, Geophys. Res. Lett., 42, 10478–10485, https://doi.org/10.1002/2015GL066544, 2015.

Zhang, Y., Stevens, B., Medeiros, B., and Ghil, M.: Low-cloud fraction, lower-tropospheric stability, and large-scale divergence, J. Climate, 22, 4827–4844, https://doi.org/10.1175/2009JCLI2891.1, 2009.

Zhou, X., Ackerman, A. S., Fridlind, A. M., Wood, R., and Kollias, P.: Impacts of solar-absorbing aerosol layers on the transition of stratocumulus to trade cumulus clouds, Atmos. Chem. Phys., 17, 12725–12742, https://doi.org/10.5194/acp-17-12725-2017, 2017.